International Journal of Solids and Structures 169 (2019) 187–204

Contents lists available at ScienceDirect

International Journal of Solids and Structures

journal homepage: www.elsevier.com/locate/ijsolstr

Pseudo-projection approach to reconstruct locations of point-like scatterers characterized by Lamé parameters and mass densities in an elastic half-space

Terumi Touhei*, Taizo Maruyama

Department of Civil Engineering, Tokyo University of Science, 2641, Yamazaki, Noda 278-8510, Japan

ARTICLE INFO

Article history:
Received 14 July 2018
Revised 3 April 2019
Available online 8 April 2019

Keywords:
Inverse scattering
Elastic half-space
MUSIC algorithm
Near-field observation
Far-field properties of Green's functions
Monopole and dipole sources
Pseudo-projections

ABSTRACT

A method for reconstructing the locations of point-like scatterers in an elastic half-space is developed in this article. Point-like scatterers are characterized by fluctuations of the Lamé parameters and the mass densities from the background structure of the wavefield. A representation of the wavefield is realized with the monopole and dipole Green's functions. The main contribution of the present work is to clarify the far-field properties of the Green's functions for both the monopole and dipole sources, which yields the pseudo-projection approach to the wave problem. Indicator functions that reconstruct the locations of point-like scatterers are defined by the far-field operator derived from the pseudo-projections and the near-field observation. Numerical computations were carried out to verify the accuracy of the pseudo-projection method. The sensitivities of the accuracy of the reconstruction results for the proposed method to random noise, the grid resolution at the free surface, and the analyzed frequency were also examined.

1. Introduction

Inverse scattering analysis techniques have been widely studied due to their inherent appeal as well as their potential applications, such as in geophysical exploration, site characterization, medical imaging, and non-destructive testing. Many significant articles in this field have already been published and the number of research articles is growing rapidly. This being the case, Colton and Kress (2018) published a review article on the development of the mathematical theory of inverse scattering analysis since the 1970s. As they mention, it is well known that sampling methods such as the linear sampling, factorization, and topological sensitivity methods, also have had important roles in the history of the development of inverse scattering analysis.

The application of the linear sampling method (Colton and Kirsch, 1996) to an elastic wavefield can be seen in Fata and Guzina (2004) and Baganas et al. (2006). They formulated the near-field equation and gave the mathematical details its properties for an elastic half-space. Pourahmadian et al. (2017) presented a generalized linear sampling method for the reconstruction of heterogeneous fractures. The factorization method Kirsch (1998) and Kirsch (2011), which clarifies the range of the far-field operator by factorization, is also a useful tool for elastic wave scattering problems. Hu et al. (2016) applied the factorization method to the solid-fluid interaction problem. (Bazán et al., 2017) applied the factorization method together with maximum product criterion (Bazán et al., 2012) to the shape reconstruction problem in an elastic wavefield. Applications of the topological sensitivity methods based on the topological derivative (Sokolowski and Zochowski, 1999) to an elastic wavefield can be seen in Ammari et al. (2013), in which they used the elastic moment tensors (Ammari and Kang, 2007). The MUSIC algorithm (e.g., Cheney, 2001) is also a sampling method which identifies the locations of scatterers. The application to the elastic wavefield of the MUSIC algorithm can be seen in Gintides et al. (2012), who reconstructed point-like scatterers in 2D full space using one type of elastic scattering wave (P or S waves). Ammari et al. (2005) applied the MUSIC algorithm to locating small electro-magnetic buried inclusions in a half-space. They also applied their method for small elastic inclusion (Ammari et al., 2008), in which the elastic moment tensor played a role in constructing the indicator function.

One of the authors of the present article also developed the pseudo-projection approach for the MUSIC algorithm (Touhei, 2018) in order to apply it to a 3D elastic half-space. The method derives the far-field operator from the near-field observation by applying the pseudo-projection, which extracts one type of wave (P, SV, or SH waves) from the wavefield in an elastic half-space. In addition, the range of the far-field operator is constructed with respect to each probing point in order to

* Corresponding author.
E-mail address: touhei@rs.noda.tus.ac.jp (T. Touhei).

https://doi.org/10.1016/j.ijsolstr.2019.04.019
0020-7683/

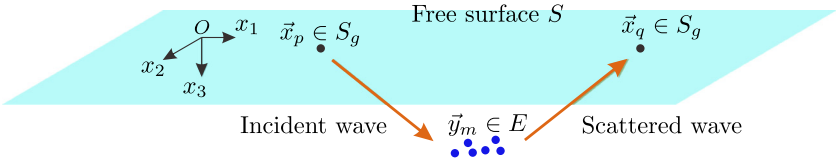

Fig. 1. Schematic of the scattering problem. An incident wave generated from a point source propagates to point-like scatterers. We observe the scattered waves propagating back to the free surface.

observe the locations of the point-like scatterers carefully. These properties of the method are expected to provide accurate imaging results and differ from those in the articles mentioned above. The method, however, was formulated for point-like scatterers characterized only by the fluctuation of the mass density from the background of the wavefield.

This article develops an inversion method for identifying locations of point-like scatterers characterized by the fluctuation not only of the mass densities but also of the Lamé parameters from the background structure of an elastic half-space. The method itself is a qualitative one as in a group of the sampling methods and is an extension of the method presented by Touhei (2018). In the previous work by one of the authors, however, the pseudo-projection was only for a Green's function due to a monopole source. In addition, the characterization of the far-field operator derived from the pseudo-projection was not complete. When dealing with point-like scatterers characterized by the fluctuation of the Lamé parameters and mass densities, Green's functions for both monopole and dipole sources are necessary. In view of the above, the task of the present article comprises the following four points:

(i) Clarify the far-field properties of the Green's functions for both monopole and dipole sources in terms of polarization vectors.
(ii) Construct the pseudo-projections for the Green's functions for both monopole and dipole sources.
(iii) Verify the factorization of the far-field operator derived from the pseudo-projections.
(iv) Characterize the range of the far-field operator derived from the pseudo-projections.

For the purpose of the task of the present article, the outline of the formulation of the present method is organized as follows: First, in Section 2.1, the problem considered in this paper is defined. In Section 2.2, a representation of a scattered wavefield by Green's functions for the monopole and dipole sources is shown. After that, the pseudo-projections for Green's functions for both the monopole and dipole sources, which are found to be the same due to the structure of the directivity tensors, are introduced in Section 2.3. In Section 2.4, the far-field operator is obtained by applying the pseudo-projections to the near-field operator in the Born regime.

2. Theoretical formulation

2.1. Definition of the scattering problem and basic equations

Fig. 1 shows the outline of the wave problem dealt with in this article. The wavefield is a 3D elastic half-space, in which the incident waves from point sources at the free surface propagate toward the point-like scatterers embedded in the half-space. We observe the scattered waves propagating back to the free surface. The problem considered in this article is how to develop a method for identifying the locations of point-like scatterers characterized by fluctuations of the Lamé parameters as well as the mass densities from the background structure of the wavefield.

The analysis is carried out in the frequency domain with time factor $\exp(-i\omega t)$, where ω is the circular frequency and t is the time. A Cartesian coordinate system is employed to express the wavefield. The components of the spatial point in terms of the Cartesian coordinates are expressed as

$$\vec{x} = (x_1, x_2, x_3) \in \mathbb{R}^2 \times \mathbb{R}_+ = \mathbb{R}^3_+ \tag{1}$$

where x_3 denotes the vertical coordinate where the positive direction is downwards and $x_3 = 0$ denotes the free surface of the elastic half-space, which is denoted by S. The subscript index for the vectors and tensors describes the components of the coordinate system and the summation convention is applied to the subscript index. We set the source and sensor grids in S to identify the location of the point-like scatterers, for which the number of grid points in S is finite. Let the set defining the source and sensor grids be denoted by

$$S_g = \{\vec{x}_p\}_{p=1}^N \subset S \tag{2}$$

where N is the number of grid points in S_g.

The Lamé parameters and the mass density are expressed as

$$\begin{aligned} \lambda(\vec{x}) &= \lambda_0 + \tilde{\lambda}(\vec{x}) \\ \mu(\vec{x}) &= \mu_0 + \tilde{\mu}(\vec{x}) \\ \rho(\vec{x}) &= \rho_0 + \tilde{\rho}(\vec{x}) \end{aligned} \tag{3}$$

where λ, μ, and ρ are the Lamé parameters and the mass density with background values λ_0, μ_0, and ρ_0 and fluctuations $\tilde{\lambda}$, $\tilde{\mu}$, and $\tilde{\rho}$.

The fluctuations are characterized by the point-like scatterers which are expressed by

$$\begin{aligned} \tilde{\lambda}(\vec{x}) &= \sum_{\vec{y}_m \in E} \tilde{\lambda}_m \delta(\vec{x} - \vec{y}_m) \\ \tilde{\mu}(\vec{x}) &= \sum_{\vec{y}_m \in E} \tilde{\mu}_m \delta(\vec{x} - \vec{y}_m) \\ \tilde{\rho}(\vec{x}) &= \sum_{\vec{y}_m \in E} \tilde{\rho}_m \delta(\vec{x} - \vec{y}_m) \end{aligned} \tag{4}$$

where $\tilde{\lambda}_m$, $\tilde{\mu}_m$ and $\tilde{\rho}_m$ are the amplitudes of the fluctuations, $\delta(\cdot)$ is the Dirac delta function, and $\vec{y}_m$ is the position of the point-like scatterers. Note that the set of point-like scatterers is denoted by E.

The S and P wave velocities for the background structure are represented by

$$\begin{aligned} c^{(1)} &= \sqrt{\frac{\lambda_0 + 2\mu_0}{\rho_0}} \\ c^{(2)} &= \sqrt{\frac{\mu_0}{\rho_0}}. \end{aligned} \tag{5}$$

The wavenumbers for the P and S waves are expressed as

$$\xi^{(1)} = \omega / c^{(1)}, \quad \xi^{(2)} = \omega / c^{(2)}. \tag{6}$$

Note that the superscripts (1) and (2) for c and ξ indicate that the physical quantities are related to the P and S waves, respectively. Later, we use the superscript (3) to indicate the physical

quantities related to SH waves. Here, the superscript (2) is for describing SV waves. For example, we sometimes use $\xi^{(2)}$ and $\xi^{(3)}$ for the wavenumbers of SV and SH waves, respectively. Regardless of the notation, we understand that

$$\xi^{(2)} = \xi^{(3)} \tag{7}$$

The Green's function for an elastic half-space is denoted by $G_{ij}(\vec{x},\vec{y})$, where the subscripts i and j describe the components of the Cartesian coordinate system, $\vec{x}$ is the field point, and $\vec{y}$ is the source point. The Green's function for an elastic half-space is defined by the following equation:

$$L_{ij}(\partial_x)G_{jk}(\vec{x},\vec{y}) = -\delta_{ik}\delta(\vec{x}-\vec{y}), \quad (\vec{x},\vec{y}\in\mathbb{R}^3_+) \tag{8}$$

$$\lim_{x_3\to 0} P_{ij}(\partial_x)G_{jk}(\vec{x},\vec{y}) = 0 \tag{9}$$

where L_{ij} is the Lamé operator defined by

$$L_{ij}(\partial_x) = (\lambda_0+\mu_0)\partial_{x_i}\partial_{x_j} + \delta_{ij}(\mu_0\partial_{x_k}\partial_{x_k} + \rho_0\omega^2) \tag{10}$$

and P_{ij} is an operator that transforms the displacement field to the traction for the x_3 plane, whose components are

$$\left[P_{ij}(\partial_x)\right] = \begin{bmatrix} \mu_0\partial_{x_3} & 0 & \mu_0\partial_{x_1} \\ 0 & \mu_0\partial_{x_3} & \mu_0\partial_{x_2} \\ \lambda_0\partial_{x_1} & \lambda\partial_{x_2} & (\lambda_0+2\mu_0)\partial_{x_3} \end{bmatrix}. \tag{11}$$

Note that ∂_{x_j} is the partial differential operator whose subscript denotes the parameter for the differentiation and δ_{ij} in Eq. (8) is the Kronecker delta. As notation for Green's functions, $G^{\nwarrow}_{ij}(\vec{x},\vec{y})$ and $G^{\swarrow}_{ij}(\vec{x},\vec{y})$ are used later to clarify the direction of the waves of a Green's function, as well as the structure of the factorization of the far-field operator derived from the pseudo-projections. The definitions for this notation are

$$\begin{aligned} G^{\nwarrow}_{ij}(\vec{x},\vec{y}) &\overset{\text{def}}{=} G_{ij}(\vec{x},\vec{y}), \text{ for } \vec{x}\in S \text{ and } \vec{y}\in\mathbb{R}^3_+\setminus S \\ G^{\swarrow}_{ij}(\vec{x},\vec{y}) &\overset{\text{def}}{=} G_{ij}(\vec{x},\vec{y}), \text{ for } \vec{x}\in\mathbb{R}^3_+\setminus S \text{ and } \vec{y}\in S \end{aligned} \tag{12}$$

According to the reciprocity of Green's functions, the following relationship can be established:

$$G^{\nwarrow}_{ij}(\vec{x},\vec{y}) = G^{\swarrow}_{ji}(\vec{y},\vec{x}), \quad \vec{x}\in S,\ \vec{y}\in\mathbb{R}^3_+\setminus S \tag{13}$$

The derivatives of Green's functions are also necessary in the following. We employ the following notation for the derivatives of Green's functions $G^{\nwarrow}_{ij}(\vec{x},\vec{y})$:

$$G^{\nwarrow}_{ij,k}(\vec{x},\vec{y}) = \partial_{y_k}G^{\nwarrow}_{ij}(\vec{x},\vec{y}), \quad (\vec{x}\in S,\ y\in\mathbb{R}^3_+\setminus S,\ k=1,2,3) \tag{14}$$

while the notation for the derivatives of Green's function $G^{\swarrow}_{ji}(\vec{y},\vec{x})$ is

$$G^{\swarrow}_{ji,k}(\vec{y},\vec{x}) = \partial_{y_k}G^{\swarrow}_{ji}(\vec{y},\vec{x}), \quad (\vec{x}\in S,\ y\in\mathbb{R}^3_+\setminus S,\ k=1,2,3). \tag{15}$$

As can be seen in the Appendix, the derivatives of Green's functions $G^{\nwarrow}_{ij,k}$ are evaluated from the dipole sources. The tensors formed by the derivatives of Green's functions are also important in the formulation of the proposed method later, which are

$$T^{\nwarrow}_{ijk}(\vec{x},\vec{y}) = (1/2)\left(G^{\nwarrow}_{ij,k}(\vec{x},\vec{y}) + G^{\nwarrow}_{ik,j}(\vec{x},\vec{y})\right) \tag{16}$$

$$T^{\swarrow}_{kji}(\vec{y},\vec{x}) = (1/2)\left(G^{\swarrow}_{ji,k}(\vec{y},\vec{x}) + G^{\swarrow}_{ki,j}(\vec{y},\vec{x})\right). \tag{17}$$

From the reciprocity and symmetry of Green's functions, the following relationship is established:

$$T^{\swarrow}_{kji}(\vec{y},\vec{x}) = T^{\nwarrow}_{ikj}(\vec{x},\vec{y}) \tag{18}$$

$$\begin{aligned} T^{\nwarrow}_{ijk}(\vec{x},\vec{y}) &= T^{\nwarrow}_{ikj}(\vec{x},\vec{y}) \\ T^{\swarrow}_{kji}(\vec{y},\vec{x}) &= T^{\swarrow}_{jki}(\vec{y},\vec{x}) \end{aligned} \tag{19}$$

2.2. Representation of the scattered wavefield

In this section, we have to clarify the representation of the scattered wavefield in the presence of fluctuations characterized by the Lamé parameters and mass densities of the wavefield. We will see how the derivatives of Green's functions can be used for the representation of the scattered wavefield. Let u_i and ϵ_{ij} be respectively the displacement field and strain tensor corresponding to the total field for the wave problem. We decompose the wavefield in the following form:

$$\begin{aligned} u_i(\vec{x}) &= u_i^{(0)}(\vec{x}) + u_i^{(s)}(\vec{x}) \\ \epsilon_{ij}(\vec{x}) &= \epsilon_{ij}^{(0)}(\vec{x}) + \epsilon_{ij}^{(s)}(\vec{x}) \end{aligned} \tag{20}$$

where a (0) superscript denotes the incident background wavefield and an (s) denotes the scattered wavefield. We employ the Born approximation in this article. Then, the decomposition of the stress tensor can be expressed as

$$\begin{aligned} \sigma_{ij}(\vec{x}) = {} & \lambda_0\delta_{ij}\epsilon_{kk}^{(0)}(\vec{x}) + 2\mu_0\epsilon_{ij}^{(0)}(\vec{x}) \\ & +\lambda_0\delta_{ij}\epsilon_{kk}^{(s)}(\vec{x}) + 2\mu_0\epsilon_{ij}^{(s)}(\vec{x}) \\ & +\tilde{\lambda}(\vec{x})\delta_{ij}\epsilon_{kk}^{(0)}(\vec{x}) + 2\tilde{\mu}(\vec{x})\epsilon_{ij}^{(0)}(\vec{x}). \end{aligned} \tag{21}$$

It is known that the scattered wavefield can be expressed by the following volume integral equation (e.g., Touhei, 2011):

$$u_i^{(s)}(\vec{x}) = \int_\Omega G_{ij}(\vec{x},\vec{y})M_{jk}(\partial_y)u_k^{(0)}(\vec{y})d\vec{y} \tag{22}$$

where Ω is an arbitrary domain which includes the region for the point-like scatterers E and M_{jk} is the operator due to the presence of the fluctuation of the wavefield expressed as

$$\begin{aligned} M_{jk}(\partial) = {} & (\tilde{\lambda}+\tilde{\mu})\partial_j\partial_k + \delta_{jk}\left(\tilde{\mu}\partial_l\partial_l + \tilde{\rho}\omega^2\right) \\ & +\partial_j\tilde{\lambda}\,\partial_k + \partial_k\tilde{\mu}\,\partial_j + \delta_{jk}\partial_l\tilde{\mu}\,\partial_l. \end{aligned} \tag{23}$$

As shown in Fig. 2, the domain Ω is surrounded by the boundary Γ and S, where $\Gamma\cap S=\emptyset$. According to the decomposition of the wavefield, Eq. (22) can be modified into

$$\begin{aligned} u_i^{(s)}(\vec{x}) = {} & \int_\Omega G^{\nwarrow}_{ij}(\vec{x},\vec{y})\left(\partial_{y_k}\left(\lambda(\vec{y})\delta_{jk}\epsilon_{ll}(\vec{y}) + 2\mu(\vec{y})\epsilon_{jk}(\vec{y})\right)\right. \\ & \left. + \rho(\vec{y})\omega^2 u_j(\vec{y})\right)d\vec{y} \\ & - \int_\Omega G^{\nwarrow}_{ij}(\vec{x},\vec{y})\left(\partial_{y_k}\left(\lambda_0\delta_{jk}\epsilon_{ll}(\vec{y}) + 2\mu_0\epsilon_{jk}(\vec{y})\right)\right. \\ & \left. + \rho_0\omega^2 u_j(\vec{y})\right)d\vec{y} \end{aligned} \tag{24}$$

In the context of the Born approximation, we have used

$$\rho(\vec{x})u_i(\vec{x}) = \rho_0 u_i(\vec{x}) + \tilde{\rho}(\vec{x})u_i^{(0)}(\vec{x}) \tag{25}$$

for Eq. (24).

Integration by parts of the first term on the right-hand side of Eq. (24) yields

$$\begin{aligned} & \int_\Omega G^{\nwarrow}_{ij}\left(\vec{x},\vec{y}\right)\left(\partial_{y_k}\left(\lambda\left(\vec{y}\right)\delta_{jk}\epsilon_{ll}\left(\vec{y}\right) + 2\mu\left(\vec{y}\right)\epsilon_{jk}\left(\vec{y}\right)\right)\right. \\ & \quad \left. +\rho\left(\vec{y}\right)\omega^2 u_j\left(\vec{y}\right)\right)d\,\vec{y} \\ & = \int_\Omega\left[-\lambda\left(\vec{y}\right)T^{\nwarrow}_{ikk}\left(\vec{x},\vec{y}\right)\epsilon_{ll}\left(\vec{y}\right) - 2\mu\left(\vec{y}\right)T^{\nwarrow}_{ikl}\left(\vec{x},\vec{y}\right)\epsilon_{kl}\left(\vec{y}\right)\right. \\ & \quad \left. +\rho\left(\vec{y}\right)\omega^2 G^{\nwarrow}_{ij}\left(\vec{x},\vec{y}\right)u_j\left(\vec{y}\right)\right]d\,\vec{y} \\ & \quad + \int_\Gamma G^{\nwarrow}_{ij}\left(\vec{x},\vec{y}\right)n_k\left(\vec{y}\right)\left[\lambda_0\delta_{jk}\epsilon_{ll}\left(\vec{y}\right) + 2\mu_0\epsilon_{jk}\left(\vec{y}\right)\right]d\Gamma\left(\vec{y}\right) \end{aligned} \tag{26}$$

where n_k is the component of the normal vector defined at the boundary Γ whose direction is outward from the region Ω. As a

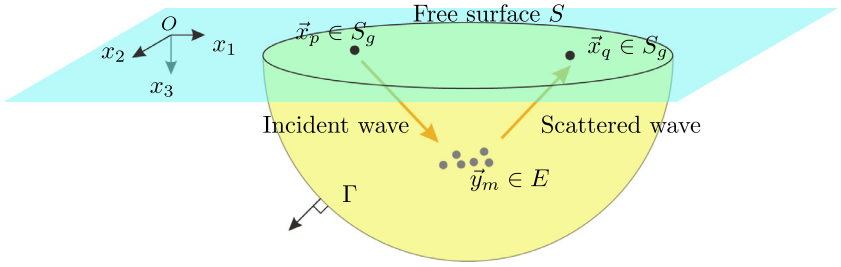

Fig. 2. Region Ω containing the point-like scatterers. Region Ω is surrounded by the boundaries Γ and S, where $\Gamma \cap S = \emptyset$. Note that applying integration by parts to Eq. (24) does not yield the boundary terms for Γ and S.

result of Eq. (26), it is not difficult to see that the boundary terms caused by the results of applying integration by parts to the first and second terms on the right-hand side of Eq. (24) cancelled each other out. Therefore, introducing Eq. (4) into the results of the integration by parts of Eq. (24) yields

$$\begin{aligned} u_i^{(s)}\left(\vec{x}\right) = &- \sum_{\vec{y}_m \in E} \tilde{\lambda}_m T_{ikk}^{\nwarrow}\left(\vec{x}, \vec{y}_m\right) \epsilon_{ll}^{(0)}\left(\vec{y}_m\right) \\ &- \sum_{\vec{y}_m \in E} 2\tilde{\mu}_m T_{ijk}^{\nwarrow}\left(\vec{x}, \vec{y}_m\right) \epsilon_{jk}^{(0)}\left(\vec{y}_m\right) \\ &+ \sum_{\vec{y}_m \in E} \tilde{\rho}_m \omega^2 G_{ij}^{\nwarrow}\left(\vec{x}, \vec{y}_m\right) u_j^{(0)}\left(\vec{y}_m\right) \end{aligned} \tag{27}$$

At this point, let the background wavefield be due to the Green's function at the source point $\vec{x}_q \in S_g$. Then, from Eq. (27), we have the representation of the kernel of the near-field operator as the following form:

$$\begin{aligned} \mathcal{N}_{ij}(\vec{x}_p, \vec{x}_q) = &- \sum_{\vec{y}_m \in E} \tilde{\lambda}_m T_{ikk}^{\nwarrow}(\vec{x}, \vec{y}_m) T_{llj}^{\swarrow}(\vec{y}_m, \vec{x}_q) \\ &- \sum_{\vec{y}_m \in E} 2\tilde{\mu}_m T_{ikl}^{\nwarrow}(\vec{x}, \vec{y}_m) T_{klj}^{\swarrow}(\vec{y}_m, \vec{x}_q) \\ &+ \sum_{\vec{y}_m \in E} \tilde{\rho}_m \omega^2 G_{ik}^{\nwarrow}(\vec{x}, \vec{y}_m) G_{kj}^{\swarrow}(\vec{y}_m, \vec{x}_q) \end{aligned} \tag{28}$$

Eq. (28) shows how the derivatives of Green's functions are used in the representation of the near-field operator. We need to evaluate $G_{ij}^{\nwarrow}$ and $T_{ijk}^{\nwarrow}$ for Eq. (28), from which $G_{ij}^{\swarrow}$ and $T_{ijk}^{\swarrow}$ are determined by the reciprocity of Green's functions.

2.3. Pseudo-projections derived from the far-field properties of Green's functions

The far-field properties of Green's functions and their derivatives are derived and summarized in the Appendix, where a Green's function and its derivatives are expressed as

$$G_{ij}^{\nwarrow}(\vec{x}, \vec{y}) = \sum_{\alpha=1}^{3} \frac{\exp(i\xi^{(\alpha)}|\vec{x}-\vec{y}|)}{4\pi|\vec{x}-\vec{y}|} D_{ij}^{\infty(\alpha)}(\theta, \varphi) + O(|\vec{x}-\vec{y}|^{-2}) \tag{29}$$

$$G_{ij,k}^{\nwarrow}(\vec{x}, \vec{y}) = \sum_{\alpha=1}^{3} \frac{\exp(i\xi^{(\alpha)}|\vec{x}-\vec{y}|)}{4\pi|\vec{x}-\vec{y}|} D_{ijk}^{\infty(\alpha)}(\theta, \varphi) + O(|\vec{x}-\vec{y}|^{-2}) \tag{30}$$

based on Eq. (A.31), where the tensors $D_{ij}^{\infty(\alpha)}$ and $D_{ijk}^{\infty(\alpha)}$, which we call the directivity tensors, are defined by Eqs. (A.35)–(A.38). Note that an 'A' in an equation number, such as Eq. (A.38), indicates an equation presented in the Appendix. The angles θ and φ define the direction of the vector $\vec{x}-\vec{y}$ as shown in Fig. 3.

The main properties of the directivity tensors are summarized in the following theorem based on Eqs. (A.39) and (A.40).

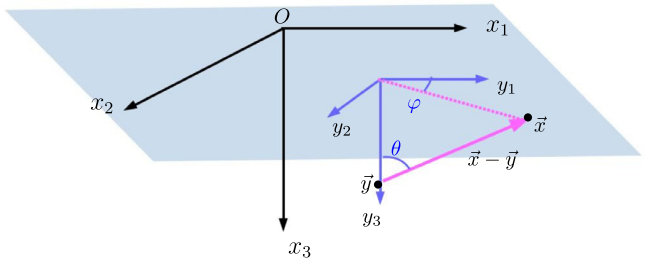

Fig. 3. Definitions of the angles θ and φ, which determine the direction of $\vec{x}-\vec{y}$.

Theorem 1. *The directivity tensors for the derivative of Green's function can be decomposed into the following form:*

$$\begin{aligned} D_{ijk}^{\infty(\alpha)}(\theta, \varphi) &= -i\xi^{(\alpha)} D_{ij}^{\infty(\alpha)}(\theta, \varphi) V_k^{(1)}(\theta, \varphi) \\ &= -i\xi^{(\alpha)} A^{(\alpha)}(\theta) W_i^{(\alpha)}(\theta, \varphi) V_j^{(\alpha)}(\theta, \varphi) V_k^{(1)}(\theta, \varphi) \end{aligned} \tag{31}$$

where $V_i^{(\alpha)}$ and $W_i^{(\alpha)}$ denote the polarizations of the elastic waves of the (α)-type wave in the full space and at the free surface, respectively, and $A^{(\alpha)}$ is the amplitude. The explicit forms of $A^{(\alpha)}$, $V_i^{(\alpha)}$, and $W_i^{(\alpha)}$ are

$$\begin{aligned} A^{(1)}(\theta) &= \frac{-2\xi_{s1}\gamma_{s1}\,(\xi_{s1}^2 + \nu_{s1}^2)}{\mu_0 F_{s1} \sin^2\theta} \\ A^{(2)}(\theta) &= \frac{2\nu_{s2}^2(\xi_{s2}^2 + \nu_{s2}^2)}{\mu_0 F_{s2} \cos^2\theta} \\ A^{(3)}(\theta) &= \frac{2}{\mu_0} \end{aligned} \tag{32}$$

$$\begin{aligned} \left(V_i^{(1)}(\theta, \varphi)\right) &= \begin{pmatrix} \cos\varphi \sin\theta & \sin\varphi \sin\theta & -\cos\theta \end{pmatrix} \\ \left(V_i^{(2)}(\theta, \varphi)\right) &= \begin{pmatrix} \cos\varphi \cos\theta & \sin\varphi \cos\theta & \sin\theta \end{pmatrix} \\ \left(V_i^{(3)}(\theta, \varphi)\right) &= \begin{pmatrix} \sin\varphi & -\cos\varphi & 0 \end{pmatrix} \end{aligned} \tag{33}$$

$$\begin{aligned} \left(W_i^{(1)}(\theta, \varphi)\right) &= \begin{pmatrix} \cos\varphi \sin\theta & \sin\varphi \sin\theta & \dfrac{i(\xi_{s1}^2 + \nu_{s1}^2)}{2\nu_{s1}\xi_{s1}} \sin\theta \end{pmatrix} \\ \left(W_i^{(2)}(\theta, \varphi)\right) &= \begin{pmatrix} \cos\varphi \cos\theta & \sin\varphi \cos\theta & \dfrac{2i\xi_{s2}\gamma_{s2}}{\xi_{s2}^2 + \nu_{s2}^2} \cos\theta \end{pmatrix} \\ \left(W_i^{(3)}(\theta, \varphi)\right) &= \left(V_i^{(3)}(\theta, \varphi)\right) \end{aligned} \tag{34}$$

where

$$\begin{aligned} \xi_{s\alpha} &= \xi^{(\alpha)} \sin\theta \\ \gamma_{s\alpha} &= \sqrt{\xi_{s\alpha}^2 - (\xi^{(1)})^2} \\ \nu_{s\alpha} &= \sqrt{\xi_{s\alpha}^2 - (\xi^{(2)})^2} \\ F_{s\alpha} &= \left(2\xi_{s\alpha}^2 - (\xi^{(2)})^2\right)^2 - 4\xi_{s\alpha}^2 \gamma_{s\alpha} \nu_{s\alpha} \end{aligned} \tag{35}$$

for $\alpha = 1, 2$.

At this point, we construct $W_i^{(\alpha\star)}$ satisfying the following properties:

$$W_i^{(\alpha)}(\theta,\varphi)W_i^{(\beta\star)}(\theta,\varphi)=\delta_{\alpha\beta}W_i^{(\alpha)}(\theta,\varphi)W_i^{(\alpha\star)}(\theta,\varphi) \tag{36}$$

The explicit forms of $W_i^{\alpha\star}$ are also given in Eq. (A.45) and are as follows:

$$\begin{aligned}\left(W_i^{(1\star)}(\theta,\varphi)\right)&=\begin{pmatrix}\cos\varphi & \sin\varphi & \dfrac{i(\xi_{s2}^2+\nu_{s2}^2)}{2\xi_{s2}\gamma_{s2}}\end{pmatrix}\\ \left(W_i^{(2\star)}(\theta,\varphi)\right)&=\begin{pmatrix}\cos\varphi & \sin\varphi & \dfrac{2i\nu_{s1}\xi_{s1}}{(\xi_{s1}^2+\nu_{s1}^2)}\end{pmatrix}\\ \left(W_i^{(3\star)}(\theta,\varphi)\right)&=\left(W_i^{(3)}(\theta,\varphi)\right)\end{aligned} \tag{37}$$

From the structure of the directivity tensors $D_{ij}^{\infty(\alpha)}$ and $D_{ijk}^{\infty(\alpha)}$ shown in Theorem 1 as well as $W_i^{(\alpha\star)}$, we reach the definition of the pseudo-projection as follows:

$$\mathcal{F}_{ij}^{(\alpha)}(\theta,\varphi)=\frac{W_i^{(\alpha)}(\theta,\varphi)\,W_j^{(\alpha\star)}(\theta,\varphi)}{W_l^{(\alpha)}(\theta,\varphi)\,W_l^{(\alpha\star)}(\theta,\varphi)},\quad(\alpha=1,2,3) \tag{38}$$

which satisfies the identity

$$\mathcal{F}_{ij}^{(\alpha)}(\theta,\varphi)\mathcal{F}_{jk}^{(\beta)}(\theta,\varphi)=\delta_{\alpha\beta}\mathcal{F}_{ik}^{(\alpha)}(\theta,\varphi) \tag{39}$$

although $\mathcal{F}_{ij}^{(\alpha)}$ is not Hermitian. The effects of the pseudo-projection on a Green's function as well as its derivatives are summarized by the following corollary derived from Theorem 1.

Corollary 1. *Pseudo-projections extract one type of wave from a Green's function as well as its derivatives as follows:*

$$\begin{aligned}&\mathcal{F}_{ij}^{(\alpha)}(\theta,\varphi)\,G_{jk}^{\nwarrow}(\vec{x},\vec{y})\\ &=\frac{\exp(i\xi^{(\alpha)}|\vec{x}-\vec{y}|)}{4\pi|\vec{x}-\vec{y}|}W_i^{(\alpha)}(\theta,\varphi)U_k^{(\alpha)}(\theta,\varphi)+O(|\vec{x}-\vec{y}|^{-2})\\ &\mathcal{F}_{ij}^{(\alpha)}(\theta,\varphi)\,T_{jkl}^{\nwarrow}(\vec{x},\vec{y})\\ &=\frac{\exp(i\xi^{(\alpha)}|\vec{x}-\vec{y}|)}{4\pi|\vec{x}-\vec{y}|}W_i^{(\alpha)}(\theta,\varphi)U_{kl}^{(\alpha)}(\theta,\varphi)+O(|\vec{x}-\vec{y}|^{-2})\end{aligned} \tag{40}$$

where

$$U_k^{(\alpha)}(\theta,\varphi)=A^{(\alpha)}(\theta)V_k^{(\alpha)}(\theta,\varphi) \tag{41}$$

$$\begin{aligned}U_{kl}^{(\alpha)}(\theta,\varphi)=&-(1/2)i\xi^{(\alpha)}A^{(\alpha)}(\theta)\\ &\times\left(V_k^{(\alpha)}(\theta,\varphi)V_l^{(1)}(\theta,\varphi)+V_l^{(\alpha)}(\theta,\varphi)V_k^{(1)}(\theta,\varphi)\right)\end{aligned} \tag{42}$$

Proof. The results of this corollary come from the straightforward calculations in Eqs. (29)–(31) and the properties of $W_i^{(\alpha\star)}$ shown in Eq. (36). □

The actions of the pseudo-projections on $G_{ij}^{\swarrow}$ as well as $T_{ijk}^{\swarrow}$ are also important. Due to the reciprocity of Green's functions, these actions are expressed as follows:

$$\begin{aligned}&\mathcal{F}_{ij}^{(\alpha)}(\theta,\varphi)G_{kj}^{\swarrow}(\vec{y},\vec{x})\\ &=\frac{\exp(i\xi^{(\alpha)}|\vec{x}-\vec{y}|)}{4\pi|\vec{x}-\vec{y}|}W_i^{(\alpha)}(\theta,\varphi)U_k^{(\alpha)}(\theta,\varphi)+O(|\vec{x}-\vec{y}|^{-2})\\ &\mathcal{F}_{ij}^{(\alpha)}(\theta,\varphi)T_{klj}^{\swarrow}(\vec{y},\vec{x})\\ &=\frac{\exp(i\xi^{(\alpha)}|\vec{x}-\vec{y}|)}{4\pi|\vec{x}-\vec{y}|}W_i^{(\alpha)}(\theta,\varphi)U_{kl}^{(\alpha)}(\theta,\varphi)+O(|\vec{x}-\vec{y}|^{-2}).\end{aligned} \tag{43}$$

Note that the angles (θ,φ) also describe the direction of the vector $\vec{x}-\vec{y}$ even for $G_{kj}^{\swarrow}(\vec{y},\vec{x})$ and $T_{klj}^{\swarrow}(\vec{y},\vec{x})$.

Remark. The role of the pseudo-projection will be clarified based on Corollary 1 together with the definition of the operator $\mathcal{P}_{ij}^{(\alpha)}$ later.

We now make some remarks on the properties of the directivity tensors. The polarization of the elastic waves of the P wave $V_k^{(1)}(\theta,\varphi)$ also describes the direction of any type of wave (namely, P, SV, or SH waves). Therefore, $V_k^{(1)}(\theta,\varphi)$ in Eq. (31) should be understood in the sense of the direction of the (α)-type wave, which is caused by differentiation of a Green's function. In addition, the traces of tensors $U_{ll}^{(2)}$ and $U_{ll}^{(3)}$ vanish:

$$U_{ll}^{(2)}(\theta,\varphi)=U_{ll}^{(3)}(\theta,\varphi)=0. \tag{44}$$

This is due to the orthogonality of the polarization of the elastic waves between the P and SV waves as well as between the P and SH waves. Eq. (44) arises from the fact that the volumetric strains caused by the SV and SH waves vanish.

2.4. Introduction of the far-field properties of the Green's function for the near-field operator

Now, we return to Eq. (28) for $\mathcal{N}_{ij}(\vec{x}_p,\vec{x}_q)$, which describes the scattered wave at $\vec{x}_p$ due to the point force acting at the free surface $\vec{x}_q$. The near-field operator is constructed from the stack of $\mathcal{N}_{ij}(\vec{x}_p,\vec{x}_q)$. We employ the following representation of the near-field operator:

$$(\mathcal{N}_{ik}f_k)(\vec{x}_p)=\sum_{q=1}^{N}\mathcal{N}_{ik}(\vec{x}_p,\vec{x}_q)f_k(\vec{x}_q),\quad(\vec{x}_p,\vec{x}_q\in S_g) \tag{45}$$

where $f_k(\cdot)\in\mathbb{C}^{3N}$ which is defined in S_g, with $\mathbb{C}^{3N}$ denoting the $3N$-dimensional complex vector space. In the following, we sometimes use the notation $(f_k(\cdot))$, where

$$(f_k(\vec{x}_p))=\left((f_k(\vec{x}_p)_{k=1,2,3}\right)_{p=1,\dots,N}\in\mathbb{C}^{3N}. \tag{46}$$

According to Eq. (28), Eq. (45) can also be expressed as

$$\begin{aligned}&(\mathcal{N}_{ik}f_k)(\vec{x}_p)\\ &=\left(\sum_{q=1}^{N}\sum_{\vec{y}_m\in E}-\tilde{\lambda}_m T_{ikk}^{\nwarrow}(\vec{x}_p,\vec{y}_m)T_{llj}^{\swarrow}(\vec{y}_m,\vec{x}_q)-2\tilde{\mu}_m T_{ikl}^{\nwarrow}(\vec{x}_p,\vec{y}_m)T_{klj}^{\swarrow}(\vec{y}_m,\vec{x}_q)\right.\\ &\qquad\left.+\tilde{\rho}_m\omega^2 G_{ik}^{\nwarrow}(\vec{x}_p,\vec{y}_m)G_{kj}^{\swarrow}(\vec{y}_m,\vec{x}_q)\right)f_j(\vec{x}_q),\qquad(\vec{x}_p,\vec{x}_q\in S_g).\end{aligned} \tag{47}$$

To introduce the far-field properties of Green's functions to the near-field operator shown in Eq. (47), let $\vec{z}_s$ be a probing point and define the following operator with respect to this probing point:

$$\mathcal{P}_{ij}^{(\alpha)}(\vec{x}_p,\vec{z}_s)=\kappa(\xi^{(\alpha)},\vec{x}_p,\vec{z}_s)\mathcal{F}_{ij}^{(\alpha)}(\theta_{ps},\varphi_{ps}) \tag{48}$$

where

$$\kappa\left(\xi^{(\alpha)},\vec{x}_p,\vec{z}_s\right)=4\pi\left|\vec{x}_p-\vec{z}_s\right|\exp\left(-i\xi^{(\alpha)}\left|\vec{x}_p-\vec{z}_s\right|\right) \tag{49}$$

and angles $(\theta_{ps},\varphi_{ps})$ define the direction of the vector $\vec{x}_p-\vec{z}_s$. In the following, we also use the notation for angles $(\theta_{pm},\varphi_{pm})$ to define the direction of the vector $\vec{x}_p-\vec{y}_m$.

The operator $\mathcal{P}_{ij}^{(\alpha)}(\vec{x}_p,\vec{z}_s)$ is now applied to the near-field operator $\mathcal{N}_{jk}$ to obtain a far-field operator. By the use of Corollary 1, which holds from the properties of pseudo-projections, characterization of the range of the far-field operator becomes possible. Namely, for the case that $\vec{z}_s\in\{\vec{y}_m\}$, the application of $\mathcal{P}_{ij}^{(\alpha)}$ yields a derived operator with a range coinciding with the directivity tensor for the α-type waves, which enables the construction of the indicator function. In order to realize the properties of the range, the operator $\mathcal{P}_{ij}^{(\alpha)}$ needs $\kappa(\xi^{(\alpha)},\vec{x}_p,\vec{z}_s)$ to eliminate the effects of

geometrical decay and the phase of the waves from the probing point.

To introduce the far-field properties of Green's function to the near-field operator and to characterize the derived far-field operator, we construct the tensors $H_{ikl}^{(\alpha)}$ and $H_{ik}^{(\alpha)}$:

$$\begin{aligned}\mathcal{P}_{il}^{(\alpha)}(\vec{x}_p,\vec{z}_s)T_{ljk}^{\nwarrow}(\vec{x}_p,\vec{y}_m) &= H_{ijk}^{(\alpha)}(\vec{x}_p,\vec{z}_s,\vec{y}_m)+O(|\vec{x}_p-\vec{z}_s||\vec{x}_p-y_m|^{-2})\\ \mathcal{P}_{il}^{(\alpha)}(\vec{x}_p,\vec{z}_s)G_{lj}^{\nwarrow}(\vec{x}_p,\vec{y}_m) &= H_{ij}^{(\alpha)}(\vec{x}_p,\vec{z}_s,\vec{y}_m)+O(|\vec{x}_p-\vec{z}_s||\vec{x}_p-y_m|^{-2})\end{aligned} \tag{50}$$

According to Eqs. (40), (48) and (50), the tensors $H_{ijk}^{(\alpha)}$ and $H_{ij}^{(\alpha)}$ can be expressed by

$$\begin{aligned}H_{ij}^{(\alpha)}(\vec{x}_p,\vec{z}_s,\vec{y}_m) &= W_i^{(\alpha)}(\theta_{ps},\varphi_{ps})\sum_{\beta=1}^{3}B^{(\alpha\beta)}(\vec{x}_p,\vec{z}_s,\vec{y}_m)U_j^{(\beta)}(\theta_{pm},\varphi_{pm})\\ H_{ijk}^{(\alpha)}(\vec{x}_p,\vec{z}_s,\vec{y}_m) &= W_i^{(\alpha)}(\theta_{ps},\varphi_{ps})\sum_{\beta=1}^{3}B^{(\alpha\beta)}(\vec{x}_p,\vec{z}_s,\vec{y}_m)U_{jk}^{(\beta)}(\theta_{pm},\varphi_{pm})\end{aligned} \tag{51}$$

where

$$\begin{aligned}&B^{(\alpha\beta)}(\vec{x}_p,\vec{z}_s,\vec{y}_m)\\ &=\frac{|\vec{x}_p-\vec{z}_s|}{|\vec{x}-\vec{y}_m|}\,\frac{\exp(i\xi^{(\beta)}|\vec{x}_p-\vec{y}_m|)}{\exp(i\xi^{(\alpha)}|\vec{x}_p-\vec{z}_s|)}\,\frac{W_k^{(\beta)}(\theta_{pm},\varphi_{pm})W_k^{(\alpha\star)}(\theta_{ps},\varphi_{ps})}{W_l^{(\alpha)}(\theta_{ps},\varphi_{ps})W_l^{(\alpha\star)}(\theta_{ps},\varphi_{ps})}.\end{aligned} \tag{52}$$

The introduction of the far-field properties of Green's function to the near-field operator is realized by $\mathcal{A}_{ij}^{\infty(\alpha)}$ which is the product of $\mathcal{P}^{(\alpha)}$ and the kernel of the near-field operator such that

$$\begin{aligned}&\mathcal{P}_{ik}^{(\alpha)}(\vec{x}_p,\vec{z}_s)\mathcal{N}_{kl}(\vec{x}_p,\vec{x}_q)\mathcal{P}_{jl}^{(\alpha)}(\vec{x}_q,\vec{z}_s)\\ &=\mathcal{A}_{ij}^{\infty(\alpha)}(\vec{z}_s)+O(|\vec{x}_p-\vec{z}_s||\vec{x}_p-\vec{y}_m|^{-2})+O(|\vec{x}_q-\vec{z}_s||\vec{x}_q-\vec{y}_m|^{-2}).\end{aligned} \tag{53}$$

Substituting Eq. (47) into Eq. (53) gives

$$\begin{aligned}&\left(\mathcal{A}_{ij}^{\infty(\alpha)}(\vec{z}_s)f_j\right)(\vec{x}_p)\\ &=\sum_{q=1}^{N}\sum_{\vec{y}_m\in E}\Big(-\tilde{\lambda}_m H_{ikk}^{(\alpha)}(\vec{x}_p,\vec{z}_s,\vec{y}_m)H_{jll}^{(\alpha)}(\vec{x}_q,\vec{z}_s,\vec{y}_m)\\ &\quad-2\tilde{\mu}_m H_{ikl}^{(\alpha)}(\vec{x}_p,\vec{z}_s,\vec{y}_m)H_{jkl}^{(\alpha)}(\vec{x}_q,\vec{z}_s,\vec{y}_m)\\ &\quad+\tilde{\rho}_m\omega^2 H_{ik}^{(\alpha)}(\vec{x}_p,\vec{z}_s,\vec{y}_m)H_{jk}^{(\alpha)}(\vec{x}_q,\vec{z}_s,\vec{y}_m)\Big)f_j(\vec{x}_q),\\ &\quad(\alpha=1,2,3).\end{aligned} \tag{54}$$

For the case that $\vec{z}_s\to\vec{y}_m$, we see that

$$B^{(\alpha\beta)}(\vec{x}_p,\vec{z}_s,\vec{y}_m)\longrightarrow\delta_{\alpha\beta} \tag{55}$$

and as a result we have

$$\begin{aligned}H_{ij}^{(\alpha)}(\vec{x}_p,\vec{z}_s,\vec{y}_m)&\longrightarrow W_i^{(\alpha)}(\theta_{pm},\varphi_{pm})U_j^{(\alpha)}(\theta_{pm},\varphi_{pm})\\ &= D_{ij}^{\infty(\alpha)}(\theta_{pm},\varphi_{pm})\\ H_{ijk}^{(\alpha)}(\vec{x}_p,\vec{z}_s,\vec{y}_m)&\longrightarrow W_i^{(\alpha)}(\theta_{pm},\varphi_{pm})U_{jk}^{(\alpha)}(\theta_{pm},\varphi_{pm})\\ &= (1/2)\left(D_{ijk}^{\infty(\alpha)}(\theta_{pm},\varphi_{pm})+D_{ikj}^{\infty(\alpha)}(\theta_{pm},\varphi_{pm})\right)\end{aligned} \tag{56}$$

for the case of $\vec{z}_s\to\vec{y}_m$. We have thus used Eqs. (A.39), (A.40), (41) and (42) to obtain Eq. (56).

We now characterize the range of the operator $\mathcal{A}_{ij}^{\infty(\alpha)}(\vec{z}_s)$.

Theorem 2. *Let $\mathcal{M}^{(\alpha)}(\vec{z}_s)$ be a subspace of $\mathbb{C}^{3N}$ such that*

$$\mathcal{M}^{(\alpha)}(\vec{z}_s)=\operatorname*{span}_{1\le k,l\le 3}\left\{\left(D_{ik}^{\infty(\alpha)}(\theta_{ps},\varphi_{ps})\right),\left(D_{ikl}^{\infty(\alpha)}(\theta_{ps},\varphi_{ps})\right)\right\} \tag{57}$$

Then, the following characterization of the range of the operator $\mathcal{A}_{ij}^{\infty(\alpha)}(\vec{z}_s)$ becomes possible:

$$\exists\,\vec{y}_{m^*}\in E \text{ such that } \vec{z}_s=\vec{y}_{m^*}\iff\mathcal{M}^{(\alpha)}(\vec{z}_s)\subset\operatorname{ran}\mathcal{A}_{ij}^{\infty(\alpha)}(\vec{z}_s) \tag{58}$$

Remark. Note that the elements in $\mathcal{M}^{(\alpha)}$ become

$$\begin{aligned}\left(D_{ik}^{\infty(\alpha)}(\theta_{ps},\varphi_{ps})\right)&=\left(\left(D_{ik}^{\infty(\alpha)}(\theta_{ps},\varphi_{ps})\right)_{i=1,2,3}\right)_{p=1,\dots,N}\in\mathbb{C}^{3N}\\ \left(D_{ikl}^{\infty(\alpha)}(\theta_{ps},\varphi_{ps})\right)&=\left(\left(D_{ikl}^{\infty(\alpha)}(\theta_{ps},\varphi_{ps})\right)_{i=1,2,3}\right)_{p=1,\dots,N}\in\mathbb{C}^{3N}\end{aligned} \tag{59}$$

for fixed k and l.

Proof. Assume that $\exists\vec{y}_{m^*}\in E$ such that

$$\vec{y}_{m^*}=\vec{z}_s; \tag{60}$$

then we have the following expression for the derived far-field operator:

$$\begin{aligned}&\left(\mathcal{A}_{ij}^{\infty(\alpha)}(\vec{z}_s)f_j\right)(\vec{x}_p)\\ &=\left(\mathcal{A}_{ij}^{\infty(\alpha)m^*}(\vec{z}_s)f_j\right)(\vec{x}_p)+\left(\overline{\mathcal{A}_{ij}^{\infty(\alpha)m^*}}(\vec{z}_s)f_j\right)(\vec{x}_p)\end{aligned} \tag{61}$$

where

$$\begin{aligned}&\left(\mathcal{A}_{ij}^{\infty(\alpha)m^*}(\vec{z}_s)f_j\right)(\vec{x}_p)\\ &=D_{ikk}^{\infty(\alpha)}(\theta_{ps},\varphi_{ps})\\ &\quad\times\sum_{q=1}^{N}-\tilde{\lambda}_{m^*}W_j^{(\alpha)}(\theta_{qs},\varphi_{qs})U_{ll}^{(\alpha)}(\theta_{qs},\varphi_{qs})f_j(\vec{x}_q)\\ &\quad+(1/2)\left(D_{ikl}^{\infty(\alpha)}(\theta_{ps},\varphi_{ps})+D_{ilk}^{\infty(\alpha)}(\theta_{ps},\varphi_{ps})\right)\\ &\quad\times\sum_{q=1}^{N}-2\tilde{\mu}_{m^*}W_j^{(\alpha)}(\theta_{qs},\varphi_{qs})U_{kl}^{(\alpha)}(\theta_{qs},\varphi_{qs})f_j(\vec{x}_q)\\ &\quad+D_{ik}^{\infty(\alpha)}(\theta_{ps},\varphi_{ps})\\ &\quad\times\sum_{q=1}^{N}\tilde{\rho}_{m^*}\omega^2W_j^{(\alpha)}(\theta_{qs},\varphi_{qs})U_k^{(\alpha)}(\theta_{qs},\varphi_{qs})f_j(\vec{x}_q)\end{aligned} \tag{62}$$

and

$$\begin{aligned}&\left(\overline{\mathcal{A}_{ij}^{\infty(\alpha)m^*}}(\vec{z}_s)f_j\right)(\vec{x}_p)\\ &=\sum_{q=1}^{N}\sum_{\vec{y}_m\in E\setminus\{\vec{y}_{m^*}\}}\Big(-\tilde{\lambda}_m H_{ikk}^{(\alpha)}(\vec{x}_p,\vec{z}_s,\vec{y}_m)H_{jll}^{(\alpha)}(\vec{x}_q,\vec{z}_s,\vec{y}_m)\\ &\quad-2\tilde{\mu}_m H_{ikl}^{(\alpha)}(\vec{x}_p,\vec{z}_s,\vec{y}_m)H_{jkl}^{(\alpha)}(\vec{x}_q,\vec{z}_s,\vec{y}_m)\\ &\quad+\tilde{\rho}_m H_{ik}^{(\alpha)}(\vec{x}_p,\vec{z}_s,\vec{y}_m)H_{jk}^{(\alpha)}(\vec{x}_q,\vec{z}_s,\vec{y}_m)\Big)f_j(\vec{x}_q)\end{aligned} \tag{63}$$

Eq. (62) can be further modified as

$$\begin{aligned}&\left(\mathcal{A}_{ij}^{\infty(\alpha)m^*}(\vec{z}_s)f_j\right)(\vec{x}_p)\\ &=D_{ikl}^{\infty(\alpha)}(\theta_{ps},\varphi_{ps})\sum_{q=1}^{N}C_{(1)jkl}^{(\alpha)}(\theta_{qs},\varphi_{qs})f_j(\vec{x}_q)\\ &\quad+D_{ik}^{\infty(\alpha)}(\theta_{ps},\varphi_{ps})\sum_{q=1}^{N}C_{(2)jkl}^{(\alpha)}(\theta_{qs},\varphi_{qs})f_j(\vec{x}_q)\end{aligned} \tag{64}$$

where

$$\begin{aligned}&C_{(1)jkl}^{(\alpha)}(\theta_{qs},\varphi_{qs})\\ &=(-\tilde{\lambda}_{m^*}\delta_{kl}U_{nn}^{(\alpha)}(\theta_{qs},\varphi_{qs})-\tilde{\mu}_{m^*}(U_{kl}^{(\alpha)}(\theta_{qs},\varphi_{qs})+U_{lk}^{(\alpha)}(\theta_{qs},\varphi_{qs})))\\ &\quad\times W_j^{(\alpha)}(\theta_{qs},\varphi_{qs})\end{aligned}$$

$$C^{(\alpha)}_{(2)jk}(\theta_{qs},\varphi_{qs}) = \tilde{\rho}_{m^*}\omega^2 U^{(\alpha)}_k(\theta_{qs},\varphi_{qs}) W^{(\alpha)}_j(\theta_{qs},\varphi_{qs}) \tag{65}$$

Eq. (64) is the factorization of the operator and we see that

$$\mathcal{M}^{(\alpha)}(\vec{z}_s) \subset \text{ran}\, \mathcal{A}^{\infty(\alpha)m^*}_{ij}(\vec{z}_s) \subset \text{ran}\, \mathcal{A}^{\infty(\alpha)}_{ij}(\vec{z}_s). \tag{66}$$

Conversely, let $\vec{z}_s \notin E$. Using Eq. (54) and following the same procedure used for deriving Eq. (64), the expression for the far-field operator is

$$\begin{aligned}
&\left(\mathcal{A}^{\infty(\alpha)}_{ij}(\vec{z}_s) f_j\right)(\vec{x}_p) \\
&= \sum_{\vec{y}_m \in E} \Bigg[W^{(\alpha)}_i(\theta_{ps},\varphi_{ps}) B^{(\alpha\beta)}(\vec{x}_p,\vec{z}_s,\vec{y}_m) A^{(\beta)}(\theta_{pm}) V^{(\beta)}_k(\theta_{pm},\varphi_{pm}) V^{(1)}_l(\theta_{pm},\varphi_{pm}) \\
&\quad \times \sum_{q=1}^{N} C^{(\alpha)}_{(3)jkl}(\vec{x}_q,\vec{z}_s,\vec{y}_m) f_j(\vec{x}_q) \\
&\quad + W^{(\alpha)}_i(\theta_{ps},\varphi_{ps}) B^{(\alpha\beta)}(\vec{x}_p,\vec{z}_s,\vec{y}_m) A^{(\beta)}(\theta_{pm}) V^{(\beta)}_k(\theta_{pm},\varphi_{pm}) \\
&\quad \times \sum_{q=1}^{N} C^{(\alpha)}_{(4)jk}(\vec{x}_q,\vec{z}_s,\vec{y}_m) f_j(\vec{x}_q) \Bigg]
\end{aligned} \tag{67}$$

where

$$\begin{aligned}
C^{(\alpha)}_{(3)jkl}(\vec{x}_q,\vec{z}_s,\vec{y}_m) &= -\tilde{\lambda}_m \delta_{kl} H^{(\alpha)}_{jnn}(\vec{x}_q,\vec{z}_s,\vec{y}_m) \\
&\quad -\tilde{\mu}_m \left(H^{(\alpha)}_{jkl}(\vec{x}_q,\vec{z}_s,\vec{y}_m) + H^{(\alpha)}_{jlk}(\vec{x}_q,\vec{z}_s,\vec{y}_m) \right) \\
C^{(\alpha)}_{(4)jk}(\vec{x}_q,\vec{z}_s,\vec{y}_m) &= \tilde{\rho}_m \omega^2 H^{(\alpha)}_{jk}(\vec{x}_q,\vec{z}_s,\vec{y}_m)
\end{aligned} \tag{68}$$

Eq. (67) is also a factorization of the operator and we see that

$$\begin{aligned}
&\left(D^{\infty(\alpha)}_{ijk}(\theta_{ps},\varphi_{ps})\right) = \left(A^{(\alpha)}(\theta_{ps}) W^{(\alpha)}_i(\theta_{ps},\varphi_{ps}) V^{(\alpha)}_j(\theta_{ps},\varphi_{ps}) V^{(1)}_k(\theta_{ps},\varphi_{ps})\right) \\
&\quad \notin \underset{\beta}{\text{span}} \left\{ \left(W^{(\alpha)}_i(\theta_{ps},\varphi_{ps}) B^{(\alpha\beta)}(\vec{x}_p,\vec{z}_s,\vec{y}_m) A^{(\beta)}(\theta_{pm}) V^{(\beta)}_j(\theta_{pm},\varphi_{pm}) V^{(1)}_k(\theta_{pm},\varphi_{pm}) \right) \right\} \\
&\left(D^{\infty(\alpha)}_{ij}(\theta_{ps},\varphi_{ps})\right) = \left(A^{(\alpha)}(\theta_{ps}) W^{(\alpha)}_i(\theta_{ps},\varphi_{ps}) V^{(\alpha)}_j(\theta_{ps},\varphi_{ps})\right) \\
&\quad \notin \underset{\beta}{\text{span}} \left\{ \left(W^{(\alpha)}_i(\theta_{ps},\varphi_{ps}) B^{(\alpha\beta)}(\vec{x}_p,\vec{z}_s,\vec{y}_m) A^{(\beta)}(\theta_{pm}) V^{(\beta)}_k(\theta_{pm},\varphi_{pm}) \right) \right\}
\end{aligned} \tag{69}$$

and as a result

$$\begin{aligned}
\left(D^{\infty(\alpha)}_{ikl}(\theta_{ps},\varphi_{ps})\right) &\notin \text{ran}\, \mathcal{A}^{\infty(\alpha)}_{ij}(\vec{z}_s) \\
\left(D^{\infty(\alpha)}_{ik}(\theta_{ps},\varphi_{ps})\right) &\notin \text{ran}\, \mathcal{A}^{\infty(\alpha)}_{ij}(\vec{z}_s).
\end{aligned} \tag{70}$$

Therefore, we have

$$\vec{z}_s = \vec{y}_{m^*} \in \{\vec{y}_m\}_{\vec{y}_m \in E} \Leftarrow \mathcal{M}^{(\alpha)}(\vec{z}_s) \subset \text{ran}\, \mathcal{A}^{\infty(\alpha)}_{ij}(\vec{z}_s) \tag{71}$$

The result then follows from Eqs. (66) and (71). □

Now, we use the following orthogonality relation:

$$\ker\left(\mathcal{A}^{\infty(\alpha)}_{ij}(\vec{z}_s)\right)^H \perp \text{ran}\, \mathcal{A}^{\infty(\alpha)}_{ij}(\vec{z}_s) \tag{72}$$

where $\left(\mathcal{A}^{\infty(\alpha)}_{ij}(\vec{z}_s)\right)^H$ is the Hermitian adjoint of the operator $\mathcal{A}^{\infty(\alpha)}_{ij}(\vec{z}_s)$. Theorem 2 and Eq. (72) allow construction of the indicator functions that reconstruct the locations of point-like scatterers. For expressing the indicator functions, we employ the following convention for the directivity tensor:

$$\left(D^{\infty(\alpha)}_{ij0}(\theta_{ps},\varphi_{ps})\right) = \left(D^{\infty(\alpha)}_{ij}(\theta_{ps},\varphi_{ps})\right) \tag{73}$$

Namely, $(D^{\infty(\alpha)}_{ij0}(\theta_{ps},\varphi_{ps}))$ denotes the directivity tensor for the monopole Green's function. Based on the above convention, we have the following four kinds of indicator functions with respect to the use of the monopole and dipole Green's functions:

$$\phi_k(\vec{z}_s) = \prod_{\alpha=1}^{3} \left[\sum_n \sum_{j=1}^{3} \left| \left(\Psi^{(\alpha)}_n(\vec{z}_s)\right)^H \left(D^{\infty(\alpha)}_{ijk}(\theta_{ps},\varphi_{ps})\right) \right|^2 \right]^{-1}, \quad (k = 0, 1, 2, 3) \tag{74}$$

where $\{(\Psi^{(\alpha)}_n(\vec{z}_s))\}_n$ is the basis for $\ker(\mathcal{A}^{\infty(\alpha)}_{ij}(\vec{z}_s))^H$. The indicator function in Eq. (74) has the following properties:

$$\lim_{\vec{z}_s \to \vec{y}_m \in E} \phi_k(\vec{z}_s) = \infty. \tag{75}$$

So far, we have shown the derivation process of the indicator function for imaging the locations of point-like scatterers. The pseudo-code for computing the indicator function is shown in Fig. 4.

As can be seen in Theorem 2, the present method has strong ties with the factorization method. The present indicator function, however, is based on the properties of the far-field operator $\mathcal{A}^{\infty(\alpha)}_{ij}(\vec{z}_s)$ defined by Eq. (53), which is defined for each probing point $\vec{z}_s$. As a result, the basis of the kernel of $(\mathcal{A}^{\infty(\alpha)}_{ij})^H$ has to be also calculated with respect to each probing point. Although this procedure is complicated, it is expected to improve the accuracy of the reconstruction of the locations of many point-like scatterers by a small number of source and sensor grid points at the free surface. As is mentioned in the Introduction, this fact marks its significant difference from other sampling methods. In the following numerical examples, the spatial spreads of the indicator functions will be investigated to examine how accurately the locations of point-like scatterers are reconstructed.

3. Numerical examples

3.1. Analysis model

The model analyzed in this section is shown in Fig. 5(a) and 5(b). We can see grid points at the free surface and point-like scatterers in the elastic half-space. The grid points at the free surface are the source and receiver sensors, for which the interval is 2.0 km and the total number of points is 121. The number of point-like scatterers for the analyzed model is 1618, which is much larger than that of the surface grid points. The point-like scatterers are spread horizontally over a 10 km × 10 km area. The source and sensor grid points at the free surface spread over an area of 20 km × 20 km, which covers the area of the point-like scatterers horizontally. The point-like scatterers are placed with a grid interval of 0.25 km, and the set of the point-like scatterers forms the shape of the object. The shape of the object is based on the salt model described in Abubakar et al. (2011). For the object, the P- and S-wave velocities are set at 4 km/s and 2.23 km/s, respectively, and the mass density is set at 2.5 g/cm^3, while the P- and S-wave velocities for the background structure of the wavefield are 2 km/s and 1 km/s, respectively, and the mass density is 2 g/cm^3. Namely, the Lamé parameters and the mass densities for the background

Near-field observation $\mathcal{N}_{ij}(\vec{x}_p, \vec{x}_q)$, $\vec{x}_p, \vec{x}_q \in S_g$

do $k = 0, \ldots, 3$
$\phi_k(\vec{z}_s) \leftarrow 1$, $(\vec{z}_s \in P)$
! P: set of probing points.
do $\alpha = 1, 3$
do $ip = 1, \ldots, nns$
! nns: number of probing points.
Select $\vec{z}_s$ according to ip

Construct the operator $\mathcal{P}_{ij}^{(\alpha)}(\vec{x}_p, \vec{z}_s)$ by Eq. (48).

Construct the far-field operator by Eq. (53):
$\mathcal{A}_{ij}^{\infty(\alpha)}(\vec{z}_s) \longleftarrow \mathcal{P}_{im}^{(\alpha)}(\vec{x}_p, \vec{z}_s)\mathcal{N}_{ml}(\vec{x}_p, \vec{x}_q)\mathcal{P}_{jl}^{(\alpha)}(\vec{x}_q, \vec{z}_s)$

Construct the basis of the kernel of the operator $\left(\mathcal{A}_{ij}^{\infty(\alpha)}(\vec{z}_s)\right)^H$
$\left\{\left(\Psi_n^{(\alpha)}(\vec{z}_s)\right)\right\}_n \longleftarrow \ker\left(\mathcal{A}_{ij}^{\infty(\alpha)}(\vec{z}_s)\right)^H$

Calculate the directivity tensors: $\left(D_{ijk}^{\infty(\alpha)}(\theta_{ps}, \varphi_{ps})\right)$

Calculate the indicator function by Eq. (74):
$\phi_k^{(\alpha)}(\vec{z}_s) = \left[\sum_n \sum_{j=1}^3 \left|\left(\Psi_n^{(\alpha))}(\vec{z}_s)\right)^H \left(D_{ijk}^{\infty(\alpha)}(\theta_{ps}, \varphi_{ps})\right)\right|^2\right]^{-1}$
$\phi_k(\vec{z}_s) \longleftarrow \phi_k(\vec{z}_s) \times \phi_k^{\alpha}(\vec{z}_s)$

enddo
enddo
enddo

Fig. 4. Pseudo-code for computing the indicator function. Note that the parameter k is used for identifying the monopole and dipole sources for the directivity tensors used for the indicator function.

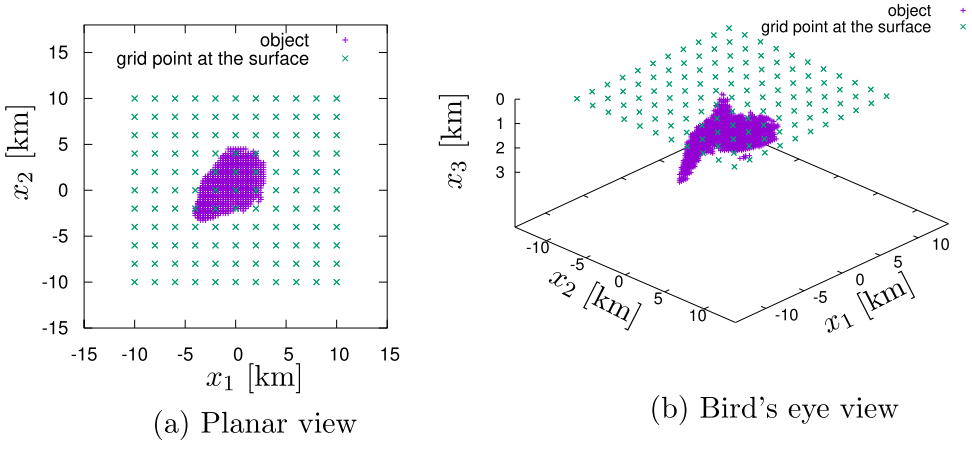

Fig. 5. Analysis model showing the source and receiver sensor grids at the free surface and the object expressed by the set of point-like scatterers in the elastic half-space.

and fluctuations of the wavefield are expressed by

$$\begin{aligned} \lambda_0 &= 4 \ \text{GPa} \\ \mu_0 &= 2 \ \text{GPa} \\ \rho_0 &= 2 \ \text{g/cm}^3 \end{aligned} \tag{76}$$

$$\begin{aligned} \tilde{\lambda} &= 11.2 \ \text{GPa} \\ \tilde{\mu} &= 10.5 \ \text{GPa} \\ \tilde{\rho} &= 0.5 \ \text{g/cm}^3. \end{aligned} \tag{77}$$

Therefore, amplitudes of the fluctuations of the Lamé parameters and the mass density in terms of Eq. (4) are obtained by multiplying Eq. (77) by $(0.25 \text{ km})^3$, where 0.25 km is the grid interval of the point-like scatterers. The results for the fluctuations of the Lamé parameters and mass density of the point-like scatterers are as follows:

$$\begin{aligned} \tilde{\lambda}_m &= 0.175 \ [\text{GPa} \cdot \text{km}^3] \\ \tilde{\mu}_m &= 0.164 \ [\text{GPa} \cdot \text{km}^3] \\ \tilde{\rho}_m &= 7.81 \times 10^9 \ [\text{kg}] \end{aligned} \tag{78}$$

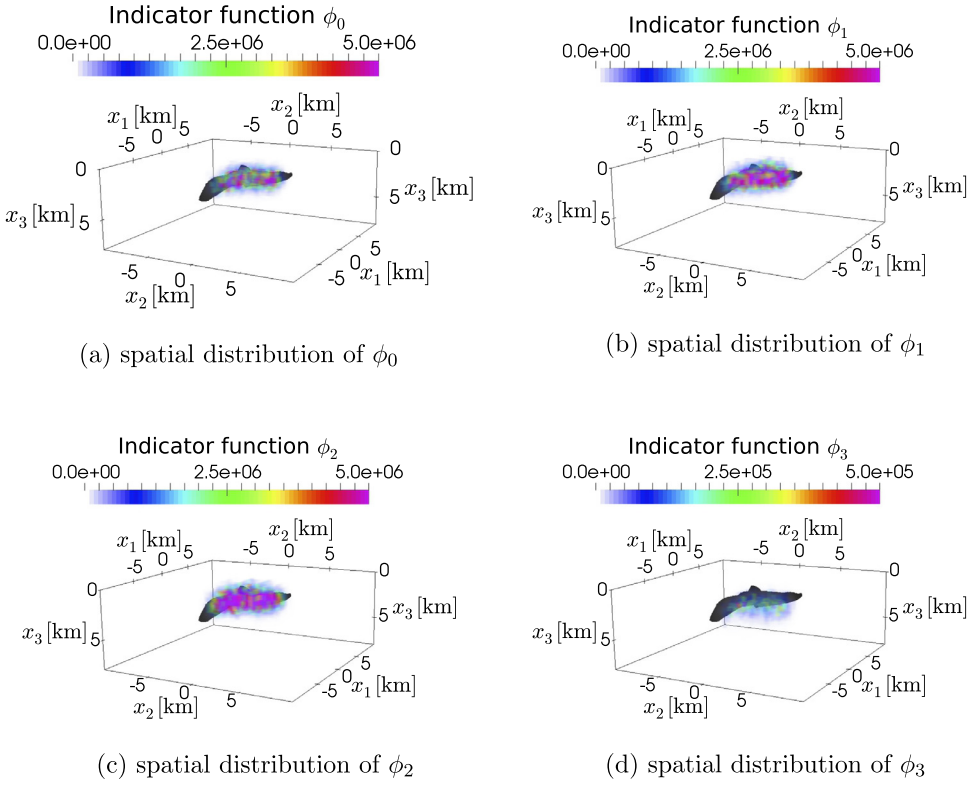

(a) spatial distribution of ϕ_0

(b) spatial distribution of ϕ_1

(c) spatial distribution of ϕ_2

(d) spatial distribution of ϕ_3

Fig. 6. Sensitivity of the indicator functions to the choice of the directivity tensors.

In the following, numerical computations are carried out to examine the accuracy of the indicator functions with respect to the choice of the directivity tensors, the analyzed frequency, random noise, and the surface sensor grid resolutions. Green's functions needed for constructing the kernel of the near-field operator shown in Eq. (28) are calculated by the direct wavenumber integrals shown in Eqs. (A.7) and (A.8). For the direct wavenumber integral, the trapezoidal formula is employed after removing the effects of the singularity of the Rayleigh pole, as is described in the Appendix. The parameters δ_1 and δ_2 defined in the Appendix are set at 1.0 km^{-1} and 0.7 km^{-1}, respectively. For the discretization of the interval $[\xi^{(2)} - \delta_2, \xi^{(2)} + \delta_2]$ for the trapezoidal formula, the increment of the wavenumber $\Delta\xi$ is set as 1×10^{-4} km^{-1}. Otherwise, $\Delta\xi$ is set as 1×10^{-2} km^{-1}.

3.2. Sensitivity to the choice of the directivity tensors in the indicator functions

Eq. (74) shows that there are four kinds of indicator functions arising from the choice of the directivity tensor for the Green's function in the indicator function. Here, we examine the sensitivity of the accuracy of the reconstruction results to the choice of the directivity tensors. Fig. 6 shows the spatial distribution of the amplitude of the indicator functions around the point-like scatterers, for which the point-like scatterers are colored dark gray. The amplitude of the indicator function is expressed by the color map. Specifically, the map describes a cloud of probing points by coloring them according to the amplitude value of the indicator function. The analyzed frequency is 0.5 Hz and the figure shows the differences between the four directivity tensors.

Fig. 6 shows that the high-amplitude area of the indicator functions agrees well with the location of the point-like scatterers, regardless of the choice of directivity tensors. A closer look at the spatial distribution of ϕ_3, which uses the directivity tensor of the dipole source around the x_3 axis, however, shows the amplitudes of the indicator function are very small when compared to other cases. Apart from this, the agreement of the high-amplitude area and the location of the point-like scatterers suggests the present method is generally valid.

3.3. Sensitivity to the analyzed frequency

It is also necessary to examine the effects of changing the analyzed frequency on the accuracy of the reconstruction results. Figs. 7 and 8 show the reconstruction results with respect to the analyzed frequencies, which are 0.5 Hz to 2.0 Hz in increments of 0.5 Hz. In these figures, the indicator functions ϕ_0 and ϕ_1 are used to illustrate the investigations. As can be seen in Figs. 7 and 8, the high-amplitude areas of the indicator functions agree well with the location of the point-like scatterers regardless of the frequency and directivity tensor considered. A closer look at the amplitudes of the indicator functions, however, shows that the amplitudes as well as the high-amplitude areas tend to decrease and become narrower as the frequencies increase. It can be said that the differences in the amplitudes of the indicator functions become smaller as the frequencies increase.

3.4. Sensitivity to random noise

In this section, we apply random noise to the near-field operator and examine the accuracy of the indicator functions when reconstructing the location of the point-like scatterers. The application of the random noise to the kernel of the near-field operator is carried out according to the following equation:

$$\widetilde{\mathcal{N}}_{ij}(\vec{x}_p, \vec{x}_q) = \mathcal{N}_{ij}(\vec{x}_p, \vec{x}_q) + \Delta_{ij}(\vec{x}_p, \vec{x}_q) \tag{79}$$

where Δ_{ij} is the random noise and $\mathcal{N}_{ij}$ is the kernel of the near-field operator defined by Eq. (28). We also define the level of noise

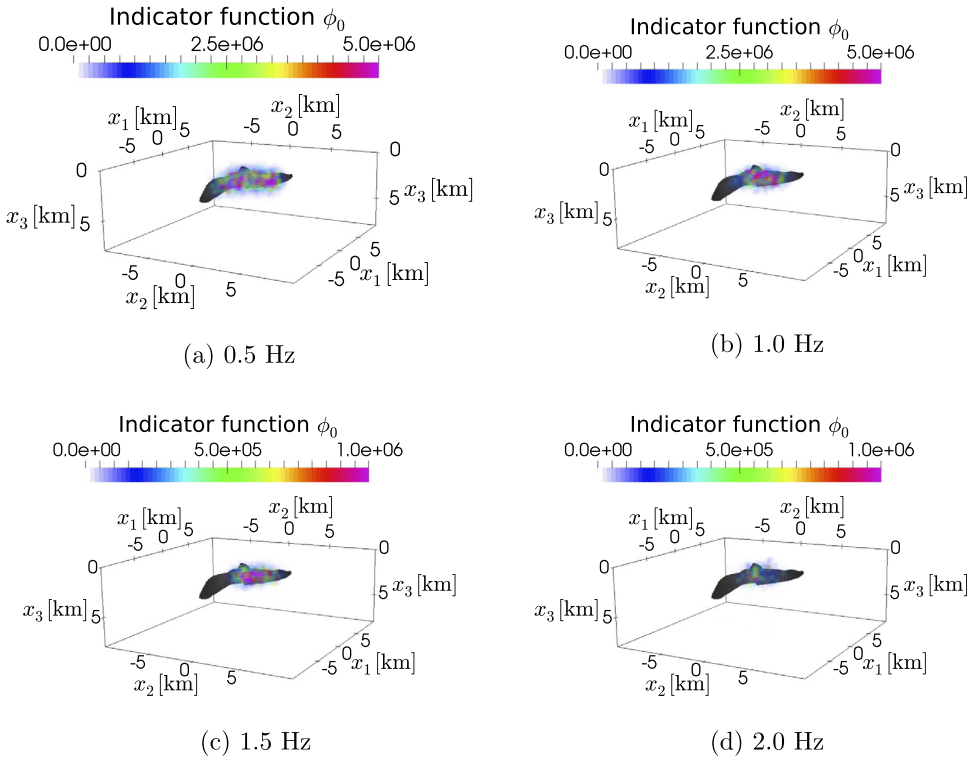

(a) 0.5 Hz (b) 1.0 Hz

(c) 1.5 Hz (d) 2.0 Hz

Fig. 7. Spatial distributions of the indicator functions for a monopole directivity tensor ($k = 0$).

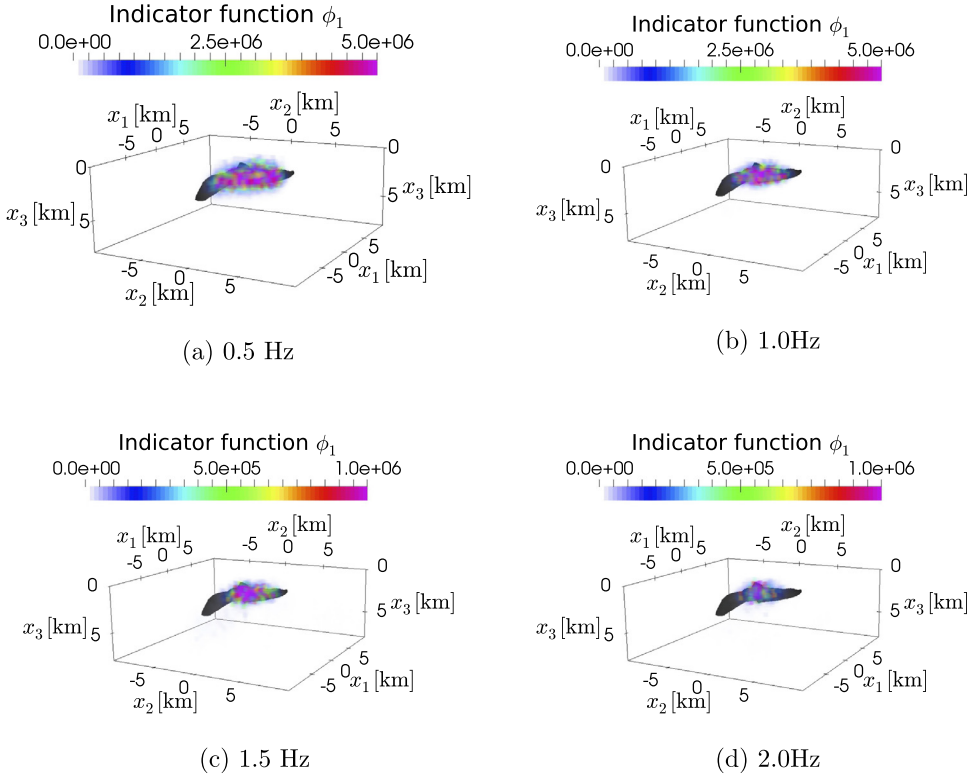

(a) 0.5 Hz (b) 1.0Hz

(c) 1.5 Hz (d) 2.0Hz

Fig. 8. Spatial distributions of the indicator functions for the dipole directivity tensor ($k = 1$).

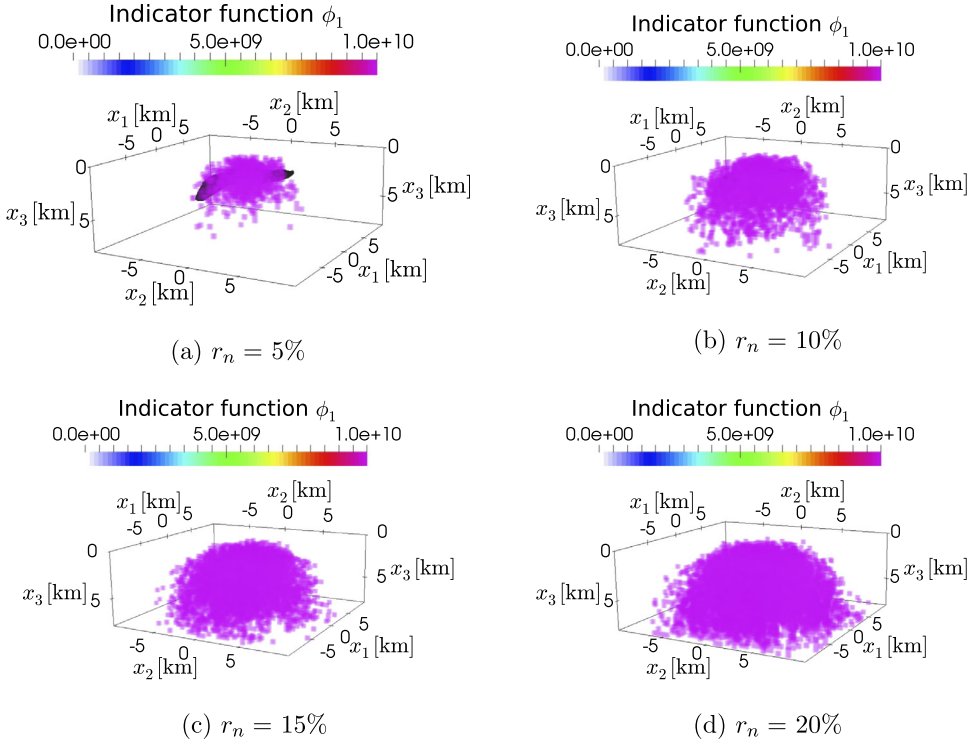

Fig. 9. Effects of introducing random noise on the accuracy of the reconstruction of the location of the point-like scatterers ($k = 1$).

r_n as follows:

$$r_n^2 = \frac{\sum_{i=1}^{3}\sum_{j=1}^{3}\sum_{\vec{x}_p\in S_g}\sum_{\vec{x}_q\in S_g}|\Delta_{ij}(\vec{x}_p,\vec{x}_q)|^2}{\sum_{i=1}^{3}\sum_{j=1}^{3}\sum_{\vec{x}_p\in S_g}\sum_{\vec{x}_q\in S_g}|\mathcal{N}_{ij}(\vec{x}_p,\vec{x}_q)|^2} \tag{80}$$

Fig. 9 shows the effects of introducing random noise on the accuracy of the reconstruction of the area of the point-like scatterers. The analyzed frequency is 0.5 Hz and the indicator function used for the analysis is ϕ_1. From Fig. 9, the spatial distribution of the high-amplitude area of the indicator function agrees well with the area of the point-like scatterers when the noise level is 5%. In this sense, this noise level does not affect the accuracy of the reconstruction of the point-like scatterers. When the noise level increases to 10% or 15%, the high-amplitude area of the indicator function agrees well with the area of the point-like scatterers; however, the amplitudes also increase outside of the point-like scatterers, especially over a deep area below the point-like scatterers. When the noise level increases to 20%, high-amplitude areas of the indicator function are scattered outside the area of the point-like scatterers and it is then difficult to identify the area. In other words, when the noise level exceeds 20%, the accuracy is insufficient. At this point, we have to remark that the described performance of the indicator function with respect to the random noise applies to the present numerical examples. Even though the described performances are associated with specific numerical examples, similar performances can be expected in comparable configurations.

3.5. Sensitivity to the sensor grid resolution

For the reconstruction of the locations of the point-like scatterers, it is desirable to have as few surface grid points as possible in order to keep the cost low. Fig. 10 shows the analyzed model

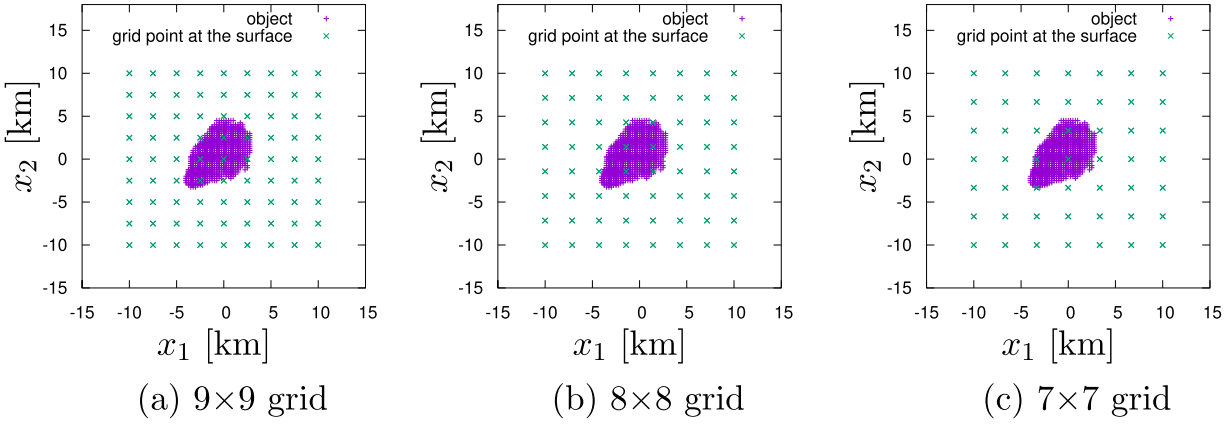

Fig. 10. Analysis model for investigating the effect of the sensor grid resolution at the free surface.

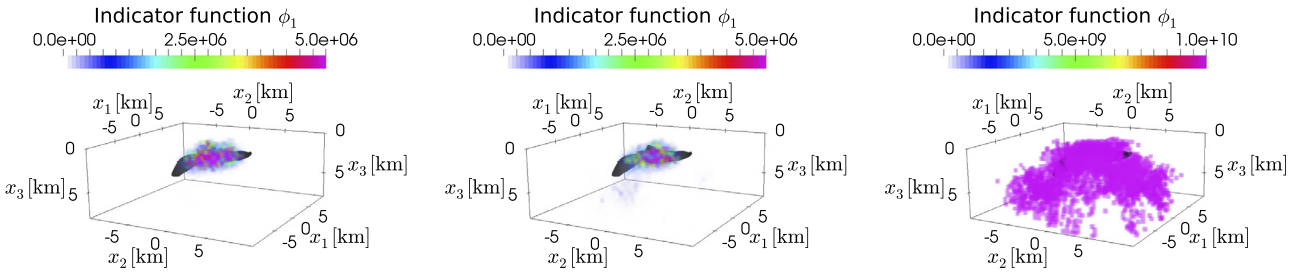

(a) 9×9 grid (b) 8×8 grid (c) 7×7 grid

Fig. 11. Sensitivity of the accuracy of the inversion to the sensor grid resolution at the free surface ($k = 1$).

for case studies examining the effects of the number of surface grid points, for which 81, 64, and 49 points were used. Fig. 11 shows the results of the identification of the area of the point-like scatterers according to surface grid resolution for an analyzed frequency of 0.5 Hz. It is found from Fig. 11 that the grid resolutions for cases (a) and (b) provide acceptable levels of accuracy. On the other hand, the grid resolution for case (c) results in a low accuracy; that is, it is not possible to reconstruct the area of the point-like scatterers with the grid resolution of case (c).

3.6. Computational cost

It is also necessary to consider the computational cost of the proposed method. Message Passing Interface parallel processing was introduced into the numerical computations by dividing the calculation points for Green's functions, as well as the number of probing points, among multiple CPU cores. An Intel Xeon E5-2690, 2.6-GHz CPU was used for the numerical computation. As mentioned earlier, the numbers of point-like scatterers and surface grid points were 1618 and 121, respectively. The number of probing points around the point-like scatterers was 26,896. The elapsed time needed for the computation for the analysis model, shown in Fig. 5, in order to obtain the near-field operator and the spatial distribution of the four kinds of indicator functions for all probing points was 92 min when 24 cores were used.

4. Conclusions

This article dealt with the reconstruction of the locations of point-like scatterers characterized by the Lamé constants as well as the mass densities in an elastic half-space. The near-field operator was represented by the monopole and dipole Green's functions. The far-field properties of the monopole and dipole Green's functions were derived from the steepest descent path method, which leads to the pseudo-projections. The pseudo-projections for the monopole and dipole Green's functions to extract one type of wave were found to be common from the structure of the directivity tensors. By means of the pseudo-projections, the near-field operator was transformed into a far-field operator that reflected the properties of one type of wave (P, SV, and/or SH waves). The indicator functions were defined from the kernel of the adjoint of the derived far-field operator with respect to each probing point. For the numerical model, the number of scatterers was much larger than the resolutions of the source and receiver sensor grids at the surface. The effects of introducing random noise and changing the surface grid resolution on the accuracy of the results were also examined. We found that the numerical results supported the validity of our method.

Appendix A. Far-field properties of the derivatives of Green's function for an elastic half-space

A1. Fourier–Hankel transform for Green's functions for monopole and dipole point sources

The purpose of this appendix is to clarify the far-field properties of derivatives of Green's function. Throughout this appendix, the wavenumbers for the P, SV, and SH waves are denoted by ξ_1, ξ_2 and ξ_3, respectively, for simplicity (note that $\xi_2 = \xi_3$). The derivatives of a Green's function can be obtained from the responses due to the dipole point sources, which can be expressed as

$$f_{ij,k}(\vec{x},\vec{y}) = \partial_{y_k} f_{ij,0}(\vec{x},\vec{y}), \quad (k = 1,2,3) \tag{A.1}$$

where $f_{ij,0}$ denotes the monopole point source defined by

$$f_{ij,0}(\vec{x},\vec{y}) = \delta_{ij}\delta(x_1 - y_1)\delta(x_2 - y_2)\delta(x_3 - y_3) \tag{A.2}$$

From Eq. (A.1), the Green's function as well as its derivatives are defined by

$$\begin{aligned} &L_{ij}(\partial_x)G_{jk,l}(\vec{x},\vec{y}) = -f_{ik,l}(\vec{x},\vec{y}) \\ &\lim_{x_3\to 0} P_{ij}(\partial_x)G_{jk,l}(\vec{x},\vec{y}) = 0 \end{aligned} \tag{A.3}$$

where $L_{ij}(\partial_x)$ is the Lamé operator and $P_{ij}(\partial_x)$ is the operator for the traction defined by Eqs. (10) and (11), respectively. As can be seen in Eq. (A.3), the Green's function due to the monopole source function is sometimes expressed by $G_{ij,0}$. The following Fourier–Hankel transform and its inverse (Touhei, 2003) can be used to solve the above Eq. (A.3):

$$\begin{aligned} \hat{u}_{(m)l}(\xi, x_3) &= \int_0^{2\pi} Q_{ik}(\varphi) \int_0^{\infty} r\left(h_{(m)lk}(\xi, r, \varphi)\right)^* u_i(\vec{x}) dr d\varphi \\ u_i(\vec{x}) &= \frac{1}{2\pi} \sum_{m=-\infty}^{\infty} Q_{ik}(\varphi) \int_0^{\infty} \xi h_{(m)kl}(\xi, r, \varphi) \hat{u}_{(m)l}(\xi, x_3) d\xi \end{aligned} \tag{A.4}$$

where u_i in this appendix is a wavefunction for an elastic half-space, $\hat{u}_{(m)i}$ is the Fourier–Hankel transform for u_i, and the superscript * denotes the complex conjugate. Here, ξ is the radial wavenumber, m is the azimuthal order number, and r and φ are defined by

$$r = \sqrt{(x_1 - y_1)^2 + (x_2 - y_2)^2},$$
$$\varphi = \tan^{-1}\frac{x_2 - y_2}{x_1 - y_1} \tag{A.5}$$

and the components for $[Q_{ik}(\varphi)]$ and $[h_{(m)kl}(\xi, r, \varphi)]$ are given as

$$[Q_{ik}(\varphi)] = \begin{bmatrix} 0 & \cos\varphi & -\sin\varphi \\ 0 & \sin\varphi & \cos\varphi \\ 1 & 0 & 0 \end{bmatrix}$$
$$\left[h_{(m)kl}(\xi, r, \varphi)\right] = \begin{bmatrix} 1 & 0 & 0 \\ 0 & \xi^{-1}\partial_r & (im)(\xi r)^{-1} \\ 0 & (im)(\xi r)^{-1} & -\xi^{-1}\partial_r \end{bmatrix} J_m(\xi r)\exp(im\varphi). \tag{A.6}$$

Note that J_m in Eq. (A.6) is the Bessel function of the first kind of mth order.

The application of the Fourier–Hankel transform defined by Eq. (A.4) to Eq. (A.3) leads to the following equation:

$$G^{\nwarrow}_{ij,k}(\vec{x}, \vec{y}) = \frac{1}{2\pi}\sum_{m=-2}^{2} Q_{il}(\varphi)\int_0^\infty \xi\, h_{(m)ln}(\xi, r, \varphi)\, g_{np}(\xi, y_3)\, \hat{\bar{f}}_{(m)pj,k}(\xi)\, d\xi, \quad (\text{when } k = 0, 1, 2) \tag{A.7}$$

$$G^{\nwarrow}_{ij,3}(\vec{x}, \vec{y}) = \frac{1}{2\pi}\sum_{m=-1}^{1} Q_{ik}(\varphi)\int_0^\infty \xi\, h_{(m)kl}(\xi, r, \varphi)\, \partial_{y_3} g_{ln}(\xi, y_3)\, \hat{\bar{f}}_{(m)nj,0}(\xi)\, d\xi \tag{A.8}$$

where $\hat{\bar{f}}$ is the Fourier–Hankel transform for $\bar{f}$ defined by

$$\bar{f}_{ik,0}(\vec{x}, \vec{y}) = \delta_{ik}\delta(x_1 - y_1)\delta(x_2 - y_2)$$
$$\bar{f}_{ik,l}(\vec{x}, \vec{y}) = \partial_{y_l}\bar{f}_{ik,0}(\vec{x}, \vec{y}), \quad (l = 1, 2) \tag{A.9}$$

and g_{ij} is a Green's function in the wavenumber domain which is decomposed into

$$[g_{ln}(\xi, y_3)] = \frac{\exp(-\gamma y_3)}{\gamma}\left[g^{(1)}_{ln}(\xi)\right] + \frac{\exp(-\nu y_3)}{\nu}\left[g^{(2)}_{ln}(\xi)\right] + \frac{\exp(-\nu y_3)}{\nu}\left[g^{(3)}_{ln}(\xi)\right] \tag{A.10}$$

where

$$\gamma = \sqrt{\xi^2 - {\xi_1}^2}$$
$$\nu = \sqrt{\xi^2 - {\xi_j}^2}, \quad (j = 2, 3) \tag{A.11}$$

The arrays for the functions are as follows:

$$\left[g^{(1)}_{ln}(\xi)\right] = \frac{1}{\mu F(\xi)}\begin{bmatrix} \gamma^2(\xi^2 + \nu^2) & -\xi\gamma(\xi^2 + \nu^2) & 0 \\ 2\xi\gamma^2\nu & -2\nu\gamma\xi^2 & 0 \\ 0 & 0 & 0 \end{bmatrix}$$
$$\left[g^{(2)}_{ln}(\xi)\right] = \frac{1}{\mu F(\xi)}\begin{bmatrix} -2\xi^2\gamma\nu & 2\xi\gamma\nu^2 & 0 \\ -\xi\nu(\xi^2 + \nu^2) & \nu^2(\xi^2 + \nu^2) & 0 \\ 0 & 0 & 0 \end{bmatrix}$$
$$\left[g^{(3)}_{ln}(\xi)\right] = \frac{1}{\mu}\begin{bmatrix} 0 & 0 & 0 \\ 0 & 0 & 0 \\ 0 & 0 & 1 \end{bmatrix} \tag{A.12}$$

where $F(\xi)$ is the Rayleigh function defined by

$$F(\xi) = \left(2\xi^2 - \xi_2^2\right)^2 - 4\xi^2\gamma\nu \tag{A.13}$$

The explicit forms of the Fourier–Hankel transforms for the dipole point source functions are as follows:

$$\left[\hat{\hat{f}}_{(m)nj,0}(\xi)\right] = \begin{cases} \begin{bmatrix} 0 & 0 & 1 \\ 0 & 0 & 0 \\ 0 & 0 & 0 \end{bmatrix} & (m=0) \\ (1/2)\begin{bmatrix} 0 & 0 & 0 \\ \pm 1 & -i & 0 \\ -i & \mp 1 & 0 \end{bmatrix} & (m=\pm 1) \\ \begin{bmatrix} 0 & 0 & 0 \\ 0 & 0 & 0 \\ 0 & 0 & 0 \end{bmatrix} & (m=\pm 2) \end{cases} \tag{A.14}$$

$$\left[\hat{\hat{f}}_{(m)nj,1}(\xi)\right] = \begin{cases} \begin{bmatrix} 0 & 0 & 0 \\ -\xi/2 & 0 & 0 \\ 0 & \xi/2 & 0 \end{bmatrix} & (m=0) \\ \begin{bmatrix} 0 & 0 & \pm\xi/2 \\ 0 & 0 & 0 \\ 0 & 0 & 0 \end{bmatrix} & (m=\pm 1) \\ \begin{bmatrix} 0 & 0 & 0 \\ \xi/4 & \mp i\xi/4 & 0 \\ \mp i\xi/4 & -\xi/4 & 0 \end{bmatrix} & (m=\pm 2) \end{cases} \tag{A.15}$$

$$\left[\hat{\hat{f}}_{(m)nj,2}(\xi)\right] = \begin{cases} \begin{bmatrix} 0 & 0 & 0 \\ 0 & -\xi/2 & 0 \\ -\xi/2 & 0 & 0 \end{bmatrix} & m=0 \\ \begin{bmatrix} 0 & 0 & -i\xi/2 \\ 0 & 0 & 0 \\ 0 & 0 & 0 \end{bmatrix} & m=\pm 1 \\ \begin{bmatrix} 0 & 0 & 0 \\ \mp i\xi/4 & -\xi/4 & 0 \\ -\xi/4 & \pm i\xi/4 & 0 \end{bmatrix} & m=\pm 2 \end{cases} \tag{A.16}$$

As is mentioned in the main text of this article, the kernel of the near-field operator defined by Eq. (28) is computed numerically from the direct wavenumber integrals for Eqs. (A.7) and (A.8). For the computation, the trapezoidal formula is used throughout after removing the effects of the singularity of the Rayleigh pole. The removal of the effects of the singularity of the Rayleigh pole is carried out using

$$\begin{aligned} &\int_0^\infty \xi\, h_{(m)ln}(\xi, r, \varphi)\, g_{np}(\xi, y_3)\, \hat{\hat{f}}_{(m)pj,k}(\xi)\, d\xi \\ &= \int_0^\infty \left(\xi\, h_{(m)ln}(\xi, r, \varphi)\, g_{np}(\xi, y_3)\, \hat{\hat{f}}_{(m)pj,k}(\xi) - \chi(\delta_1, \xi_R) \frac{A_R}{\xi - \xi_R} \right) d\xi + \text{P.V.} \int_{\xi_R-\delta_1}^{\xi_R+\delta_1} \frac{A_R}{\xi - \xi_R} d\xi + \pi i A_R \end{aligned} \tag{A.17}$$

where ξ_R is the Rayleigh pole, A_R is defined by

$$A_R = \lim_{\xi \to \xi_R} (\xi - \xi_R) \xi\, h_{(m)ln}(\xi, r, \varphi)\, g_{np}(\xi, y_3)\, \hat{\hat{f}}_{(m)pj,k}(\xi) \tag{A.18}$$

χ is the function defined by

$$\chi(\delta_1, \xi_R) = \begin{cases} 1 & \text{when} \quad \xi_R - \delta_1 \le \xi \le \xi_R + \delta_1 \\ 0 & \text{otherwise} \end{cases} \tag{A.19}$$

for a small $\delta_1 > 0$ and P.V. denotes the Cauchy principal value. The trapezoidal formula is applied to the 1st term of the right-hand side of Eq. (A.17). Note that a smaller wavenumber increment for the trapezoidal formula is necessary for an interval that contains $\xi^{(2)}$ than that for other intervals due to a weak singularity of ν^{-1} in the integrand. The interval containing $\xi^{(2)}$ is denoted by $[\xi^{(2)} - \delta_2, \xi^{(2)} + \delta_2]$ for a small $\delta_2 > 0$. In the main text, the values for δ_1 and δ_2 and the increment of the wavenumber for the trapezoidal formula are specified for the numerical integration.

A2. Application of the steepest descent path method to the wavenumber integral representation of Green's functions

Application of the steepest descent path method to the direct wavenumber integral representation of Green's functions is the key for the derivation of the far-field properties of Green's functions. First, we modify Eqs. (A.7) and (A.8) as follows:

$$G^{\nwarrow}_{ij,k}(\vec{x}, \vec{y}) = \frac{1}{4\pi} \sum_{m=-2}^{2} Q_{il}(\varphi) \int_{-\infty}^{\infty} \xi\, h_{(m1)ln}(\xi, r, \varphi)\, g_{np}(\xi, y_3)\, \hat{f}_{(m)pjk}(\xi)\, d\xi, \quad (\text{when } k = 0, 1, 2)$$

$$G^{\nwarrow}_{ij,3}(\vec{x},\vec{y}) = \frac{1}{4\pi}\sum_{m=-1}^{1} Q_{ik}(\varphi)\int_{-\infty}^{\infty} \xi\, h_{(m1)kl}(\xi, r, \varphi)\, \partial_{y_3} g_{ln}(\xi, y_3)\hat{f}_{(m)nj0}(\xi)\, d\xi \tag{A.20}$$

where

$$\left[h_{m(1)kl}(\xi : r, \varphi)\right] = \begin{bmatrix} 1 & 0 & 0 \\ 0 & \xi^{-1}\partial_r & im(\xi r)^{-1} \\ 0 & im(\xi r)^{-1} & -\xi^{-1}\partial_r \end{bmatrix} H_m^{(1)}(\xi r)\exp(im\varphi) \tag{A.21}$$

In the above expression, the following properties of the Bessel functions are used:

$$\begin{aligned} J_m(\xi r) &= \frac{1}{2}\left[H_m^{(1)}(\xi r) + H_m^{(2)}(\xi r)\right] \\ H_m^{(1)}(-\xi r) &= -H_m^{(2)}(\xi r), \quad (m : \text{even}) \\ H_m^{(1)}(-\xi r) &= H_m^{(2)}(\xi r), \quad (m : \text{odd}) \end{aligned} \tag{A.22}$$

where $H_m^{(\tau)}(\cdot)$ is the Hankel function of order m.

Now, according to the decomposition of a Green's function shown in Eq. (A.10), we can also decompose the derivatives of a Green's function with respect to the contributions from P, SV, and SH waves such that

$$G^{\nwarrow}_{ij,k}(\vec{x},\vec{y}) = \sum_{\alpha=1}^{3} G^{\nwarrow(\alpha)}_{ij,k}(\vec{x},\vec{y}). \tag{A.23}$$

For example, $G^{\nwarrow(1)}_{ij,k}(\vec{x},\vec{y})$ can be expressed as

$$\begin{aligned} &G^{\nwarrow(1)}_{ij,k}(\vec{x},\vec{y}) \\ &\quad = \frac{1}{4\pi}\sum_{m=-2}^{2} Q_{il}(\varphi)\int_{-\infty}^{\infty} \xi\, h_{(m1)ln}(\xi, r, \varphi)\, \frac{e^{-\gamma y_3}}{\gamma}\, g^{(1)}_{np}(\xi)\, \hat{f}_{(m)pj,k}(\xi)\, d\xi. \end{aligned} \tag{A.24}$$

The asymptotic behavior of the horizontal wavefunction becomes

$$h_{m(1)kl}(\xi, r, \varphi) = \sqrt{\frac{2}{\pi\xi r}} e^{i\xi r} e^{im\varphi} e^{-i\pi(2m+1)/4}\, \zeta_{kl} + O(r^{-3/2}) \tag{A.25}$$

where

$$[\zeta_{kl}] = \begin{bmatrix} 1 & 0 & 0 \\ 0 & i & 0 \\ 0 & 0 & -i \end{bmatrix}. \tag{A.26}$$

Then, each component of the waves (P, SV, and SH waves) for the derivatives of the Green's function is expressed as

$$\begin{aligned} &G^{\nwarrow(\alpha)}_{ij,k}(\vec{x},\vec{y}) \\ &\quad = \frac{1}{4\pi}\sqrt{\frac{2}{\pi r}}\sum_{m} K_{il}(\varphi) e^{im\varphi} e^{-i\pi(2m+1)/4}\int_{-\infty}^{\infty} \sqrt{\xi}\, E^{(\alpha)}(\xi, r, y_3, k)\; g^{(\alpha)}_{ln}(\xi)\, \hat{\tilde{f}}_{(m)njk}(\xi)\, d\xi \\ &\qquad + O(r^{-3/2}) \end{aligned} \tag{A.27}$$

where

$$\begin{aligned} [K_{il}(\varphi)] &= \left[Q_{ij}(\varphi)\right]\left[\zeta_{jl}\right] \\ &= \begin{bmatrix} 0 & i\cos\varphi & i\sin\varphi \\ 0 & i\sin\varphi & -i\cos\varphi \\ 1 & 0 & 0 \end{bmatrix} \end{aligned} \tag{A.28}$$

$$E^{(\alpha)}(\xi, r, y_3, k) = \begin{cases} \dfrac{\exp(i\xi r - \gamma y_3)}{\gamma} & \text{when } \alpha = 1 \text{ and } k = 0, 1, 2 \\ \dfrac{\exp(i\xi r - \nu y_3)}{\nu} & \text{when } \alpha = 2, 3 \text{ and } k = 0, 1, 2 \\ -\exp(i\xi r - \gamma y_3) & \text{when } \alpha = 1 \text{ and } k = 3 \\ -\exp(i\xi r - \nu y_3) & \text{when } \alpha = 2, 3 \text{ and } k = 3 \end{cases} \tag{A.29}$$

The path of the wavenumber integral in the complex wavenumber plane for the application of the steepest descent path method is shown in Fig. A.1, in which the saddle point on the real axis is denoted in blue.

In the following discussion, we employ the notation ξ_{s1} and ξ_{s2} for the saddle points of the P and S waves, respectively. The relationship between the saddle point and the P and S wavenumber is

$$\xi_{s1} = \xi_1 \sin\theta$$

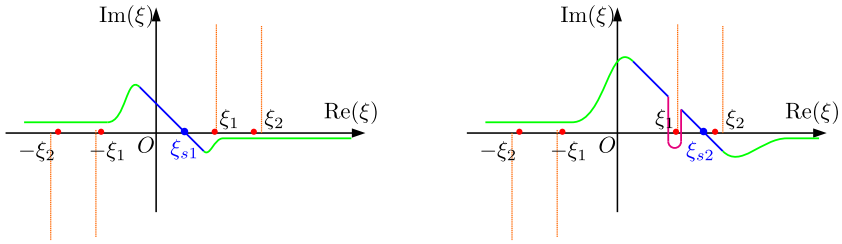

(a) Path of integral (case 1) (b) Path of integral (case 2)

Fig. A.1. Steepest descent paths. The path for case 1 describes the P and S waves when $\xi_{s2} < \xi_1$. The path for case 2 describes the S wave when $\xi_1 < \xi_{s2}$. The branch line integral for the S-P wave is required for case 2. Note that the blue segments of the integral path follow the steepest descent path and the red segment denotes the integral path around the branch cut. In addition, the broken lines are the branch cut.

$$\xi_{s2} = \xi_2 \sin\theta \tag{A.30}$$

where θ is determined by the relative locations of $\vec{x}$ and $\vec{y}$, which are explained in Fig. 3 in the main text of this article. The steepest descent paths are also described by the blue lines in Fig. A.1. Note that there is a case where $\xi_{s2} > \xi_1$. In this case, an integral path B around the branch point ξ_1 is required, as shown in case 2 in Fig. A.1. In addition, we have to take into account the contribution from the Rayleigh pole. It is known that a Green's function is expressed by the contributions from the residual term related to the Rayleigh pole, the steepest descent path, and the branch line integral. When the region of E is far enough below the free surface, the contribution from the Rayleigh wave mode to Green's function $G_{ij}^{\nwarrow}$ can be ignored, since the Rayleigh wave mode decays exponentially with depth. Furthermore, the contribution from the branch line integral shows a geometrical decay of $O(R^2)$ when $R = |\vec{x} - \vec{y}|$. As a result, the Green's function can be approximated by the contribution from the steepest descent path that shows the geometrical rate of decay $O(|\vec{x} - \vec{y}|^{-1})$ becoming

$$G_{ij,k}^{\nwarrow}(\vec{x}, \vec{y}) = \sum_{\alpha=1}^{3} \frac{e^{i\xi_\alpha |\vec{x}-\vec{y}|}}{4\pi |\vec{x}-\vec{y}|} D_{ijk}^{\infty(\alpha)}(\theta, \varphi) + O(|\vec{x}-\vec{y}|^{-2}) \tag{A.31}$$

where D_{ijk} is the directivity tensor defined by

$$D_{ijk}^{\infty(\alpha)}(\theta, \varphi) = 2K_{il}(\varphi) \sum_m e^{im\varphi} e^{-im\pi/2} \left[g_{ln}^{(\alpha)}(\xi) \hat{\tilde{f}}_{(m)njk}(\xi) \right]_{\xi = \xi_\alpha \sin\theta} \tag{A.32}$$

for $k = 0, 1, 2$ and

$$D_{ij3}^{\infty(\alpha)}(\theta, \varphi) = 2K_{il}(\varphi) \sum_m e^{im\varphi} e^{-im\pi/2} \left[-\eta^{(\alpha)} g_{ln}^{(\alpha)}(\xi) f_{nj3}^{(m)} \right]_{\xi = \xi_\alpha \sin\theta} \tag{A.33}$$

for $k = 3$. Note that

$$\eta^{(\alpha)} = \begin{cases} \gamma & (\text{when } \alpha = 1) \\ \nu & (\text{when } \alpha = 2 \text{ or } 3) \end{cases} \tag{A.34}$$

In the following, the directivity tensor $D_{ij0}^{\infty(\alpha)}$ is simply expressed by $D_{ij}^{\infty(\alpha)}$. A straightforward calculation for these equations yields the following:

$$\begin{aligned}
\left[D_{ij}^{\infty(\alpha)}(\theta, \varphi)\right] &= 2 \begin{bmatrix} g_{22}^{(\alpha)}(\xi_{s\alpha}) \cos^2\varphi & g_{22}^{(\alpha)}(\xi_{s\alpha}) \cos\varphi \sin\varphi & i g_{21}^{(\alpha)}(\xi_{s\alpha}) \cos\varphi \\ g_{22}^{(\alpha)}(\xi_{s\alpha}) \cos\varphi \sin\varphi & g_{22}^{(\alpha)}(\xi_{s\alpha}) \sin^2\varphi & i g_{21}^{(\alpha)}(\xi_{s\alpha}) \sin\varphi \\ -i g_{12}^{(\alpha)}(\xi_{s\alpha}) \cos\varphi & -i g_{12}^{(\alpha)}(\xi_{s\alpha}) \sin\varphi & g_{11}^{(\alpha)}(\xi_{s\alpha}) \end{bmatrix} \\
\left[D_{ij}^{\infty(3)}(\theta, \varphi)\right] &= 2 \begin{bmatrix} \sin^2\varphi & -\cos\varphi \sin\varphi & 0 \\ -\cos\varphi \sin\varphi & \cos^2\varphi & 0 \\ 0 & 0 & 0 \end{bmatrix} g_{33}^{(3)}(\xi_{s3})
\end{aligned} \tag{A.35}$$

$$\begin{aligned}
\left[D_{ij1}^{\infty(\alpha)}(\theta, \varphi)\right] &= -2i\xi_{s\alpha} \begin{bmatrix} g_{22}^{(\alpha)}(\xi_{s\alpha}) \cos^3\varphi & g_{22}^{(\alpha)}(\xi_{s\alpha}) \cos^2\varphi \sin\varphi & i g_{21}^{(\alpha)}(\xi_{s\alpha}) \cos^2\varphi \\ g_{22}^{(\alpha)}(\xi_{s\alpha}) \cos^2\varphi \sin\varphi & g_{22}^{(\alpha)}(\xi_{s\alpha}) \cos\varphi \sin^2\varphi & i g_{21}^{(\alpha)}(\xi_{s\alpha}) \cos\varphi \sin\varphi \\ -i g_{12}^{(\alpha)}(\xi_{s\alpha}) \cos^2\varphi & -i g_{12}^{(\alpha)}(\xi_{s\alpha}) \cos\varphi \sin\varphi & g_{11}^{(\alpha)}(\xi_{s\alpha}) \cos\varphi \end{bmatrix} \\
\left[D_{ij1}^{\infty(3)}(\theta, \varphi)\right] &= -2i\xi_{s3} g_{33}(\xi_{s3}) \begin{bmatrix} \cos\varphi \sin^2\varphi & -\cos^2\varphi \sin\varphi & 0 \\ -\cos^2\varphi \sin\varphi & \cos^3\varphi & 0 \\ 0 & 0 & 0 \end{bmatrix}
\end{aligned} \tag{A.36}$$

$$\left[D_{ij2}^{\infty(\alpha)}(\theta, \varphi)\right] = -2i\xi_{s\alpha} \begin{bmatrix} g_{22}^{(\alpha)}(\xi_{s\alpha}) \cos^2\varphi \sin\varphi & g_{22}^{(\alpha)}(\xi_{s\alpha}) \cos\varphi \sin^2\varphi & i g_{21}^{(\alpha)}(\xi_{s\alpha}) \cos\varphi \sin\varphi \\ g_{22}^{(\alpha)}(\xi_{s\alpha}) \cos\varphi \sin^2\varphi & g_{22}^{(\alpha)}(\xi_{s\alpha}) \sin^3\varphi & i g_{21}^{(\alpha)}(\xi_{s\alpha}) \sin^2\varphi \\ -i g_{12}^{(\alpha)}(\xi_{s\alpha}) \cos\varphi \sin\varphi & -i g_{12}^{(\alpha)}(\xi_{s\alpha}) \sin^2\varphi & g_{11}^{(\alpha)}(\xi_{s\alpha}) \sin\varphi \end{bmatrix}$$

$$\left[D^{\infty(3))}_{ij2}(\theta,\varphi)\right] = -2i\xi_{s3}g_{33}(\xi_{s3})\begin{bmatrix} \sin^3\varphi & -\sin^2\varphi\,\cos\varphi & 0 \\ -\cos\varphi\,\sin^2\varphi & \cos^2\varphi\,\sin\varphi & 0 \\ 0 & 0 & 0 \end{bmatrix} \tag{A.37}$$

$$\left[D^{\infty(\alpha)}_{ij3}(\theta,\varphi)\right] = -2\eta^{(\alpha)}(\xi_{s\alpha})\begin{bmatrix} g^{(\alpha)}_{22}(\xi_{s\alpha})\cos^2\varphi & g^{(\alpha)}_{22}(\xi_{s\alpha})\cos\varphi\,\sin\varphi & ig^{(\alpha)}_{21}(\xi_{s\alpha})\cos\varphi \\ g^{(\alpha)}_{22}(\xi_{s\alpha})\cos\varphi\,\sin\varphi & g^{(\alpha)}_{22}(\xi_{s\alpha})\sin^2\varphi & ig^{(\alpha)}_{21}(\xi_{s\alpha})\sin\varphi \\ -ig^{(\alpha)}_{12}(\xi_{s\alpha})\cos\varphi & -ig^{(\alpha)}_{12}(\xi_{s\alpha})\sin\varphi & g^{(\alpha)}_{11}(\xi_{s\alpha}) \end{bmatrix}$$

$$\left[D^{\infty(3)}_{ij3}(\theta,\varphi)\right] = -2\nu(\xi_{s3})g_{33}(\xi_{s3})\begin{bmatrix} \sin^2\varphi & -\cos\varphi\,\sin\varphi & 0 \\ -\cos\varphi\,\sin\varphi & \cos^2\varphi & 0 \\ 0 & 0 & 0 \end{bmatrix}. \tag{A.38}$$

In Eqs. (A.35)–(A.38), α takes a value of 1 or 2. A straightforward application of Eqs. (A.35)–(A.38) leads to the following decomposition of the directivity tensor:

$$D^{\infty(\alpha)}_{ij}(\theta,\varphi) = A^{(\alpha)}(\theta)W^{(\alpha)}_i(\theta,\varphi)V^{(\alpha)}_j(\theta,\varphi) \tag{A.39}$$

$$D^{\infty(\alpha)}_{ijk}(\theta,\varphi) = -i\xi_\alpha\, A^{(\alpha)}(\theta)\, W^{(\alpha)}_i(\theta,\varphi)\, V^{(\alpha)}_j(\theta,\varphi)\, V^{(1)}_k(\theta,\varphi) \tag{A.40}$$

where $V^{(\alpha)}_i$ denotes the polarization of elastic waves of the (α)-type wave (namely, P, SV, or SH waves) in the full space, $W^{(\alpha)}_i$ is the polarization of elastic waves of the (α)-type wave at the free surface, and $A^{(\alpha)}$ is defined by

$$\begin{aligned} A^{(1)}(\theta) &= \frac{2g^{(1)}_{22}(\xi_{s1})}{\sin^2\theta} \\ A^{(2)}(\theta) &= \frac{2g^{(2)}_{22}(\xi_{s2})}{\cos^2\theta} \\ A^{(3)}(\theta) &= 2g^{(3)}_{33}(\xi_{s3}). \end{aligned} \tag{A.41}$$

The explicit forms of $V^{(\alpha)}_i$ and $W^{(\alpha)}_i$ are

$$\begin{aligned} \left(V^{(1)}_i(\theta,\varphi)\right) &= \begin{pmatrix} \cos\varphi\sin\theta & \sin\varphi\sin\theta & -\cos\theta \end{pmatrix} \\ \left(V^{(2)}_i(\theta,\varphi)\right) &= \begin{pmatrix} \cos\varphi\cos\theta & \sin\varphi\cos\theta & \sin\theta \end{pmatrix} \\ \left(V^{(3)}_i(\theta,\varphi)\right) &= \begin{pmatrix} \sin\varphi & -\cos\varphi & 0 \end{pmatrix} \end{aligned} \tag{A.42}$$

$$\begin{aligned} \left(W^{(1)}_i(\theta,\varphi)\right) &= \left(\cos\varphi\sin\theta \quad \sin\varphi\sin\theta \quad i\frac{g^{(1)}_{12}(\xi_1\sin\theta)}{g^{(1)}_{22}(\xi_1\sin\theta)}\sin\theta\right) \\ \left(W^{(2)}_i(\theta,\varphi)\right) &= \left(\cos\varphi\cos\theta \quad \sin\varphi\cos\theta \quad i\frac{g^{(2)}_{12}(\xi_2\sin\theta)}{g^{(2)}_{22}(\xi_2\sin\theta)}\cos\theta\right) \\ \left(W^{(3)}_i(\theta,\varphi)\right) &= \left(V^{(3)}_i(\theta,\varphi)\right). \end{aligned} \tag{A.43}$$

In the main text of this article, Eqs. (A.39) and (A.40) are summarized in Theorem 1.

The following orthogonality relationship exists among the polarizations of the elastic waves of the (α)-type waves in the full space:

$$V^{(\alpha)}_i(\theta,\varphi)V^{(\beta)}_i(\theta,\varphi) = \delta_{\alpha\beta} \tag{A.44}$$

On the other hand, it is impossible to establish an orthogonality relationship among the polarizations of the elastic waves of the (α)-type waves at the free surface due to the interaction of the P-SV waves. Instead of establishing an orthogonality relationship among $W^{(\alpha)}_i$, we define $W^{(\alpha(\star)}_i(\theta,\varphi)$ as follows:

$$\begin{aligned} \left(W^{(1\star)}_i(\theta,\varphi)\right) &= \left(\cos\varphi \quad \sin\varphi \quad i\frac{g^{(2)}_{22}(\xi_2\sin\theta)}{g^{(2)}_{12}(\xi_2\sin\theta)}\right) \\ \left(W^{(2\star)}_i(\theta,\varphi)\right) &= \left(\cos\varphi \quad \sin\varphi \quad i\frac{ig^{(1)}_{22}(\xi_1\sin\theta)}{g^{(1)}_{12}(\xi_1\sin\theta)}\right) \\ \left(W^{(3\star)}_i(\theta,\varphi)\right) &= \left(W^{(3)}_i(\theta,\varphi)\right) \end{aligned} \tag{A.45}$$

Then, the orthogonality relationship among $W^{(\alpha)}_i$ and $W^{(\alpha\star)}_i$ becomes

$$W^{(\alpha)}_i(\theta,\varphi)W^{(\beta\star)}_i(\theta,\varphi) = \delta_{\alpha\beta}\, W^{(\alpha)}_i(\theta,\varphi)W^{(\alpha\star)}_i(\theta,\varphi) \tag{A.46}$$

which leads to the definition of the pseudo-projections.

References

Abubakar, A., Pan, G., Li, M., Zhang, L., Habashy, T.M., van den Berg, P., 2011. Three-dimensional seismic full-waveform inversion using the finite-difference contrast source inversion method. (Special Issue: Modelling Methods for Geophysical Imaging: Trends and Perspective). Geophys. Prospect. 59, 874–888.

Ammari, H., Bretin, E., Garnier, J., Jing, W., Kang, H., Wahab, A., 2013. Localization, stability, and resolution of topological derivative based imaging functionals in elasticity. SIAM J. Imaging Sci. 6 (4), 2174–2212.

Ammari, H., Calmon, P., Iakovleva, E., 2008. Direct elastic imaging of a small inclusion. SIAM J. Imaging Sci. 1 (2), 169–187.

Ammari, H., Iakovleva, E., Lesselier, D., 2005. A MUSIC algorithm for locating small inclusions buried in a half-space from the scattering amplitude at a fixed frequency. Multiscale Model. Simul. 3 (3), 597–628.

Ammari, H., Kang, H., 2007. Polarization and moment tensors with applications to inverse problems and effective medium theory. Applied Mathematical Sciences, Vol. 162. Springer.

Baganas, K., Guzina, B.B., Charalambopoulos, A., Manolis, D.G., 2006. A linear sampling method for the inverse transmission problem in near-field elastodynamics. Inverse Probl. 22, 1835–1853.

Bazán, F.S.V., Francisco, J.B., Leem, K.H., Pelekanos, G., 2012. A maximum product criterion as a Tikhonov parameter choice rule for Kirsch's factorization method. J. Comput. Appl. Math. 236, 4264–4275.

Bazán, F.S.V., Francisco, J.B., Leem, K.H., Pelekanos, G., Sevroglou, V., 2017. A numerical reconstruction method in inverse elastic scattering. Inverse Probl. Sci. Eng. doi:10.1080/17415977.2016.1273919.

Cheney, M., 2001. The linear sampling method and the MUSIC algorithm. Inverse Probl. 17, 591–595.

Colton, D., Kirsch, A., 1996. A simple method for solving inverse scattering problems in the resonance region. Inverse Probl. 12, 383–393.

Colton, D., Kress, R., 2018. Looking back on inverse scattering theory. SIAM Rev. 60 (4), 779–807.

Fata, S.N., Guzina, B.B., 2004. A linear sampling method for near-field inverse problems in elastodynamics. Inverse Probl. 20, 713–736.

Gintides, D., Sini, M., Thành, N.T., 2012. Detection of point-like scatterers using one type of scattered elastic waves. J. Comput. Appl. Math. 236, 2137–2145.

Hu, G., Kirsch, A., Yin, T., 2016. Factorization method in inverse interaction problems with bi-periodic interfaces between acoustic and elastic waves. Inverse Probl. Imaging doi:10.3934/ipi.2016.10.103.

Kirsch, A., 1998. Characterization of the shape of a scattering obstacle using the spectral data of the far field operator. Inverse Probl. 14, 1489.

Kirsch, A., 2011. The Factorization Method for Inverse Problems. Newton Institute. http://www.newton.ac.uk/files/seminar/20110728090009451-152765.pdf.

Pourahmadian, F., Guzina, B.B., Haddar, H., 2017. Generalized linear sampling method for elastic-wave sensing of heterogeneous fractures. Inverse Probl. 33 (5).

Sokolowski, J., Zochowski, A., 1999. On the topological derivatives in shape optimizations. SIAM J. Control Optim. 37, 1251–1272.

Touhei, T., 2003. Analysis of scattering waves in an elastic layered medium by means of the complete eigenfunction expansion form of the Green's function. Int.J. Solids Struct. 40, 3347–3377.

Touhei, T., 2011. A fast volume integral equation method for elastic wave propagation in a half space. Int. J. Solids Struct. 48, 3194–3208.

Touhei, T., 2018. Inversion of point-like scatterers in an elastic half-space by the application of the far-field properties of the Green's function to the near-field operator. Int. J. Solids Struct. 112–124.